Journal of Computational Physics 539 (2025) 114252

Contents lists available at ScienceDirect

Journal of Computational Physics

journal homepage: www.elsevier.com/locate/jcp

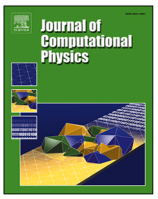

A coupled volume-of-fluid/pressure-correction method for incompressible gas-liquid flows with phase change

Michael S. Dodd, Pablo Trefftz-Posada, Antonino Ferrante *

William E. Boeing Department of Aeronautics & Astronautics, University of Washington, Seattle, WA, 98195, USA

ARTICLE INFO

Keywords:
Pressure-correction method, volume of fluid method
Phase change
Evaporation
Condensation
Multiphase flow
Mass transfer
Heat transfer

ABSTRACT

We have developed a pressure-correction method, FastP*PC, for simulating incompressible gas-liquid flows with phase change, as an extension of FastP*. The gas-liquid interface is captured using a volume-of-fluid (VoF) method that is mass conserving also in the presence of evaporation and condensation. The method relies on a divergence-free extrapolation of the gas- and liquid-phase velocity fields in the vicinity of the interface between the two fluids. This allows using any VoF algorithm for incompressible flows while the resulting numerical solution automatically keeps the boundedness and conservation properties of the chosen VoF method. The approach also has the advantage of not requiring the solution of an additional Poisson or Helmholtz equation for the entire computational domain at each time step, which is often encountered in existing methods. The results show that the interface position is computed with a spatial accuracy between first and second order. The method also applies a normal-probe approach to compute the mass flux due to phase change with second-order accuracy. Furthermore, we present a novel discretization of the vapor-species mass conservation equation for interfacial flows with phase change and a new numerical method to solve the energy equation. The flow solver maintains a sharp representation of the interface in the sense that jumps in velocity, pressure, temperature gradient, and VoF function occur over only one computational cell. A new analytical solution for verification is presented for a one-dimensional Stefan flow problem with multi-component gas phase. We apply the method to a three-dimensional evaporating droplet in quiescent conditions and demonstrate that the droplet diameter follows the D^2-law and that the solution approaches the analytical asymptotic value of the Sherwood number.

1. Introduction

In this paper we consider incompressible gas-liquid flows in which the liquid phase is monocomponent (e.g. water) and the gas phase is bicomponent (e.g. air and water vapor) as shown in Fig. 1. The liquid phase is allowed to change phase – either through evaporation or condensation or both. The gas phase is assumed to be insoluble in the liquid phase. A particular challenge in simulating these flows numerically is to capture or track the gas-liquid interface during phase change. The main computational difficulty is that the fluid velocity is discontinuous across the gas-liquid interface leading to the discrete velocity field having local non-zero divergence ($\nabla \cdot \mathbf{u} \neq 0$) . Also, the interface velocity is different than both the local liquid and gas velocities such that simply using the gas- or liquid-phase velocity to transport the interface would be incorrect.

* Corresponding author.
E-mail addresses: mchl.dodd@gmail.com (M.S. Dodd), ptrefftz@uw.edu (P. Trefftz-Posada), ferrante@aa.washington.edu (A. Ferrante).

https://doi.org/10.1016/j.jcp.2025.114252
Received 1 October 2024; Received in revised form 13 June 2025; Accepted 21 July 2025
Available online 23 July 2025

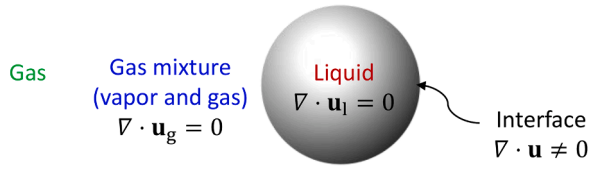

Fig. 1. Sketch of an incompressible gas-liquid flow with an evaporating droplet.

In the past, this additional complexity has been handled by extensions or modifications of interface-tracking and interface-capturing algorithms for incompressible flow [1]. For example, the front-tracking method has been used for simulating droplet vaporization [2]. In [2], the mass flux is treated as a source term at the interface in the vapor mass fraction equation. As another example, the level-set method has been used for simulating boiling flows [3–5] and droplet vaporization [5,6]. In [3–5], the interface velocity is computed from the mass balance equation at the interface. The interface velocity is then used to advect the level set function. On the other hand, in [6], the level-set function is first advected by extending the liquid velocity into the gas phase and then the phase change is accounted for by adding a term that accounts for the surface regression velocity. In the first step, the extended liquid velocity is approximated using constant extrapolation and then projected onto divergence-free space to ensure that mass is conserved. This projection requires the solution of an additional Poisson equation for a pseudo-pressure field. A similar approach has been used with a volume of fluid (VoF) scheme for modeling the free-surface flow in the vicinity of bubbles [7]. More recently, an edge-based interface-tracking (EBIT) method has been extended to simulate multiphase flows with phase change in 2D with density ratio up to 1600 [8]. The Dirichlet boundary condition for temperature at the interface is sharply imposed using the geometric information from the EBIT method. The ghost fluid method is used to address numerical instability that arise from the discontinuous velocity across the interface. The method shows second-order spatial accuracy in tracking the location of the interface in 1D test-cases, and for the bubble radius in 2D test-cases when compared with theoretical solutions or experimental results. However, the EBIT method does not guarantee mass conservation (reported errors in [8] are of $\mathcal{O}(10^{-3}, 10^{-4})$), as it is a front-tracking method, and incurs density calculation errors from piecewise linear interface reconstruction used to compute the volume fraction [8].

The VoF method has also been applied to simulate film boiling and droplet evaporation [9–11]. One approach is to directly solve the continuity equation to update the fluid density and then compute the volume fraction from the cell density [12]. This method can be extended to flows with phase change by including a source or sink term in the continuity equation [9]. However, numerical diffusion leads to smearing of the interface over time. Another approach, that is justifiable for high liquid-gas density ratios, is to assume that the liquid velocity and interface velocity are equal. This assumption was used by [10] for simulating evaporating droplets with $\rho_l/\rho_g = \mathcal{O}(10^3)$. In [11], the VoF function is advected using a combination of the liquid and gas velocity, in which, to account for phase change, the authors introduce source and sink terms on either side of the interface to ensure mass conservation. These terms are smoothed by solving an inhomogeneous Helmholtz equation to achieve numerical stability. Recently, some VoF-based numerical methods have been developed for simulating multiphase flows with phase chage [13–23]. One difficulty of using VoF-based numerical methods for simulating phase change is that the VoF advection algorithms require a divergence-free velocity for mass conservation, and phase change at the interface causes the local velocity to have non-zero divergence. One approach for handling this difficulty is to extend the liquid velocity across the interface to achieve a divergence-free velocity for advecting the VoF function [18,20–23]. Even when using an extended liquid velocity to advect the VoF function, it is challenging to ensure mass conservation when simulating phase change. Some methods employ redistribution of the VoF field to ensure mass conservation [19,21–23]. The calculation of the mass flux term is another important term to be considered for numerical methods simulating phase change. Simulations are typically performed for the evaporation limit or boiling limit of vaporization. In the evaporation limit, the vaporization rate is assumed to be limited by the local values in the vapor species [19,20]. In the boiling limit, the vaporization rate is assumed to be limited by the local values in temperature [13,15–17,21–23]. In [18], a method was developed to simulate phase change without either of the limiting assumptions for the calculation of the mass flux, but poor convergence of the liquid velocity was observed. More recently, two methods were developed for simulating multicomponent droplet evaporation which address the challenges of coupling the transport equations of multiple species in the gas and liquid phases [24,25]. The VoF method for vaporizing multicomponent droplets in [25] shows second-order spatial accuracy in capturing the location of the interface in 1D test-cases, and for the bubble radius in 2D test-cases using analytical solutions and other CFD studies, with density ratio up to 1600. However, for the case of density ratio equal to 10 for which mass conservation is reported, the method has a mass conservation error of $\mathcal{O}(10^{-1}, 10^{-2})$.

Another important issue in developing a VoF-based solver for flows with phase change is to demonstrate grid convergence of the numerical solution and report its convergence rates. Previous studies have reported the convergence rates of a few flow variables. Table 1 provides, in chronological order, a summary of VoF-based numerical methods for simulating phase change in monocomponent fluids, and their order of spatial accuracy for different quantities. A variety of test cases were conducted for the reported references, so we include the highest order of convergence reported in their work. Table 1 shows the average order of convergence for the present work. One of the objectives of the present work is to present test cases in which the results can be compared with analytical solutions, while assessing the convergence rates for the interface position, evaporation rate, and profiles of temperature, velocity and vapor mass fraction. To that end, we provide a new analytical solution for the vapor mass fraction and energy equation, which can be used to establish the accuracy of methods for gas-liquid flows with evaporation and condensation.

Table 1
Summary of spatial orders of accuracy of VoF methods for monocomponent fluids with phase change for the following variables: mass, mass flux, temperature, vapor mass fraction, and velocity. For the cited references, the highest order of accuracy of their test-cases is reported, while for the present work we report its average values. Also, for the present work, 1D errors are computed using the L_1 norm, and 2D errors are computed using the L_2 norm.

Reference	Spatial Order of Accuracy								
	Mass		Mass Flux	Temperature		Vapor Mass Fraction		Velocity	
	1D	2D	1D	1D	2D	1D	2D	1D	2D
Lee et al. [13]	2	2	1	–	–	–	–	–	–
Palmore & Desjardins [18]	–	–	–	1	1	1	1	1	< 1
Scapin et al. [20]	–	–	2	–	–	–	–	–	–
Germes Martinez et al.[21]	–	–	2	–	–	–	–	-	-
Bureš & Sato [22]	1	1.5	–	–	–	–	–	–	–
Present work	$\epsilon_{machine}$	3.51	2.19	0.98	1.47	2.09	1.39	$\epsilon_{machine}$	1.29

In the present work, for simulating incompressible gas-liquid flows with phase change, we have developed a pressure-correction method, FastP*PC, as an extension of the FastP* method [26], coupled with an extension of the VoF algorithm [27]. This VoF method uses a split advection scheme and conserves mass with an accuracy determined by the extent to which the liquid velocity field, used for the advection of the VoF function, is divergence-free in its discretized form. This condition is ensured through a new divergence-free liquid velocity extrapolation procedure. Our objective is to advance the method to simulate incompressible flows with phase change with the aim that the algorithm has the following properties:

1. conserves mass to machine precision or to a specified tolerance, and maintains boundedness of the VoF function,
2. maintains a sharp representation of the interface,
3. requires no additional solutions for the entire computational domain of elliptic PDEs (i.e. Helmholtz or Poisson equations),
4. requires no smoothing or ad-hoc redistribution of mass source/sink terms at the interface,
5. capable of handling both evaporation and condensation,
6. parallelizes easily and efficiently.

When considering a bicomponent gas mixture, there is the additional challenge of solving the vapor mass conservation equation. In this work, we assume that the gas is insoluble in the liquid. Therefore the vapor mass fraction must only be solved for in the gas phase. At the interface, either a Dirichlet boundary condition may be applied [6] or a vapor source term is introduced using a discrete Dirac delta function [10]. Our method uses the Dirichlet boundary condition at the interface, but instead of using a second-order ghost-fluid method [28] as in [6], we present a new approach that can achieve an arbitrarily high order of accuracy. Furthermore, we introduce a new approach for computing the distance from the interface for VoF-based methods.

The paper is organized as follows: in Section 2, we present the governing equations for incompressible gas-liquid flows with phase change. Section 3 presents FastP*PC, a coupled VoF and pressure-correction method used to solve the governing equations, which is an extension of the FastP* method [26] to flows with phase change. This section also includes a method for computing the mass flux due to phase change, and the discretization of the vapor mass fraction and energy equations. Section 4 presents the results obtained using FastP*PC for several verification test-cases, including a new analytical solution of the 1D Stefan flow.

2. Governing equations

We write the dimensionless governing equations for gas-liquid flows with phase change using the one-fluid formulation, under the following assumptions:

- both liquid and gas phase are incompressible,
- the liquid phase is monocomponent,
- the gas-phase is bicomponent, consisting of an inert gas and the liquid vapor,
- the gas is insoluble in the liquid,
- the production of internal energy by viscous dissipation is negligible.

A representative control volume containing the gas-liquid interface is shown in Fig. 2. It shows the gas phase, $\mathcal{V}_g$, and liquid phase, $\mathcal{V}_l$, separated by the interface, Σ.

Continuity equation:

$$\nabla \cdot \mathbf{u} = \frac{1}{\mathrm{Re\,Sc}} \left(\frac{1}{\rho_g} - \frac{1}{\rho_l} \right) \dot{m}'' \, \delta_\Sigma, \tag{1}$$

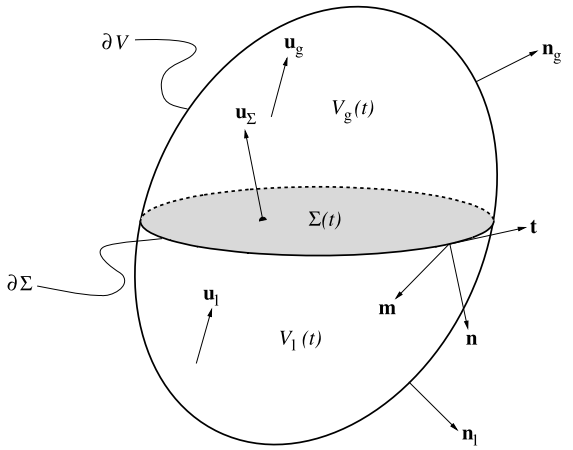

Fig. 2. Control volume $\mathcal{V}(t)$ containing an interface $\Sigma(t)$ separating the gas and liquid phases, $\mathcal{V}_g(t)$ and $\mathcal{V}_l(t)$, respectively.

which applies to $\mathcal{V}_g$, $\mathcal{V}_l$, and Σ, where $\mathbf{u}$ is the fluid velocity, ρ_g and ρ_l are the gas and liquid-phase densities, respectively, and $\dot{m}''$ is the non-dimensional mass flux due to phase change,

$$\dot{m}'' = \frac{\rho_g}{1 - Y_v} \nabla Y_v \cdot \mathbf{n}, \tag{2}$$

where Y_v is the vapor mass fraction, $\mathbf{n}$ is a unit normal directed into the liquid phase, and δ_Σ is a surface Dirac δ-function which is non-zero only at the interface (see Appendix B of [29] for a formal definition). We use the sign convention that $\dot{m}'' > 0$ during evaporation and $\dot{m}'' < 0$ during condensation. Eq. (2) is obtained from writing the total mass flux of the vapor as the sum of the convective mass flux due to Stefan flow and the diffusive mass flux described by Fick's first law of diffusion, and solving such equation for $\dot{m}''$.

Momentum equation:

$$\rho\left(\frac{\partial \mathbf{u}}{\partial t} + (\mathbf{u} \cdot \nabla)\mathbf{u}\right) = -\nabla p + \frac{1}{\mathrm{Re}} \nabla \cdot \left(\mu(\nabla \mathbf{u} + \nabla \mathbf{u}^T)\right) + \frac{1}{\mathrm{We}} \mathbf{f}_\sigma, \tag{3}$$

which applies to $\mathcal{V}_g$, $\mathcal{V}_l$, and Σ, where p is the pressure, μ is the dynamic viscosity, and $\mathbf{f}_\sigma$ is the non-dimensional force due to surface tension,

$$\mathbf{f}_\sigma = \kappa \mathbf{n} \delta_\Sigma, \tag{4}$$

where κ is the interface curvature.

Energy equation:

$$\rho c_p \left(\frac{\partial T}{\partial t} + (\mathbf{u} \cdot \nabla) T\right) = \frac{1}{\mathrm{Re\ Pr}} [\nabla \cdot (k \nabla T)] - \frac{1}{\mathrm{Re\ Sc\ Ste}} \dot{m}'' \delta_\Sigma, \tag{5}$$

which applies to $\mathcal{V}_g$, $\mathcal{V}_l$, and Σ, where c_p is the specific heat at constant pressure, T is the temperature, k is the thermal conductivity, and the last term is the sink (source) of internal energy due to evaporation (condensation).

Gas-phase vapor mass conservation equation:

$$\frac{\partial Y_v}{\partial t} + (\mathbf{u}_g \cdot \nabla) Y_v = \frac{1}{\mathrm{Re\ Sc}} \nabla^2 Y_v, \tag{6}$$

which applies to $\mathcal{V}_g$, where $\mathbf{u}_g$ is the gas phase velocity. The fluid properties, ρ, μ, c_p, and k are treated as constants in the gas and liquid phases, i.e. they are not temperature or mixture dependent. In Eqs. (1), (3), (5), and (6), Re, Sc, We, Pr, and Ste are the Reynolds, Schmidt, Weber, Prandtl, and Stefan numbers, respectively, defined as:

$$\mathrm{Re} = \frac{\tilde{U} \tilde{L} \tilde{\rho}_g}{\tilde{\mu}_g}, \quad \mathrm{Sc} = \frac{\tilde{\mu}_g}{\tilde{D}_{gv} \tilde{\rho}_g}, \quad \mathrm{We} = \frac{\tilde{\rho}_g \tilde{U}^2 \tilde{L}}{\tilde{\sigma}}, \quad \mathrm{Pr} = \frac{\tilde{\mu}_g \tilde{c}_{p,g}}{\tilde{k}_g}, \quad \mathrm{Ste} = \frac{\tilde{c}_{p,g} \tilde{T}_g}{\Delta \tilde{h}_v}, \tag{7}$$

where $\tilde{U}$, $\tilde{L}$, $\tilde{\rho}_g$, $\tilde{\mu}_g$, $\tilde{\sigma}$, $\tilde{c}_{p,g}$, $\tilde{k}_g$, $\tilde{T}_g$, $\Delta \tilde{h}_v$, and $\tilde{D}_{gv}$ denote, in order, the reference dimensional velocity, length, density, dynamic viscosity, surface tension coefficient, specific heat at constant pressure, thermal conductivity, temperature, latent heat of vaporization, and mass diffusivity of vapor in the gas phase used to non-dimensionalize the governing equations. The reference density, viscosity, specific heat, and thermal conductivity are chosen to be that of the gas, making their corresponding non-dimensional values unity in the gas phase (e.g., $\rho_g = 1$). The reference temperature is chosen to be the initial ambient gas temperature, therefore the non-dimensional

temperature of the gas phase is initially unity. Throughout the paper, all variables are dimensionless unless they are accented with ∼.

As depicted in Fig. 2, the interface velocity is denoted by $\mathbf{u}_\Sigma$ and is commonly written in terms of its normal and tangential components as

$$\mathbf{u}_\Sigma = (\mathbf{u}_\Sigma \cdot \mathbf{n})\mathbf{n} + (\mathbf{u}_\Sigma \cdot \mathbf{t})\mathbf{t}. \tag{8}$$

The continuity equation at the interface reduces to the jump conditions for the normal velocity across the interface

$$\rho_g(\mathbf{u}_\Sigma - \mathbf{u}_g)\cdot\mathbf{n} = \rho_l(\mathbf{u}_\Sigma - \mathbf{u}_l)\cdot\mathbf{n} = \frac{1}{\mathrm{Re\ Sc}}\dot{m}''. \tag{9}$$

Using Eq. (9), the normal component of $\mathbf{u}_\Sigma$ can be written as

$$\mathbf{u}_\Sigma \cdot \mathbf{n} = \frac{1}{\mathrm{Re\ Sc}}\frac{\dot{m}''}{2}\left(\frac{1}{\rho_l} + \frac{1}{\rho_g}\right) + \frac{1}{2}\left(\mathbf{u}_l + \mathbf{u}_g\right)\cdot\mathbf{n}. \tag{10}$$

3. Numerical methods

The governing Eq. (1)–(6) are discretized on a staggered Cartesian grid in three dimensions (3D) with the u-component of velocity located at $\mathbf{x}_{i+1/2,j,k}$, the v-component at $\mathbf{x}_{i,j+1/2,k}$, the w-component at $\mathbf{x}_{i,j,k+1/2}$, and all other variables centered at $\mathbf{x}_{i,j,k}$. The volume fraction field, $C(\mathbf{x},t)$, has value $C=0$ in the gas phase, $C=1$ in the liquid phase, and $0<C<1$ in computational cells containing the interface. For brevity, we will only present the 2D spatial discretization for the description of the numerical methods, while the results section includes 3D cases. All spatial derivatives are discretized using the second-order central difference scheme, except the normal gradient of the vapor mass fraction and the fluxes of vapor species near the interface, which will be discussed in Sections 3.4 and 3.5, respectively. Fig. 3 summarizes the structure and ordering of the flow solver. The time step (Δt) must be restricted to ensure numerical stability. Δt is calculated as

$$\Delta t \leq \frac{1}{2}\min(\Delta t_c, \Delta t_\nu, \Delta t_\sigma, \Delta t_m, \Delta t_e), \tag{11}$$

where $\Delta t_c, \Delta t_\nu, \Delta t_\sigma, \Delta t_m$ and Δt_e are the maximum allowable time steps due to convection, momentum diffusion, surface tension, diffusion of vapor mass-fraction and diffusion of internal energy, respectively. These are determined as suggested in [20]:

$$\begin{aligned}
\Delta t_c &= \frac{\Delta x}{|U|_{\max}} \\
\Delta t_\nu &= \frac{\mathrm{Re}\ \Delta x^2}{6} \\
\Delta t_\sigma &= \sqrt{\frac{\mathrm{We}(\rho_l+\rho_g)\Delta x^3}{4\pi}} \\
\Delta t_m &= \frac{\mathrm{Re\ Sc}\ \Delta x^2}{6} \\
\Delta t_e &= \frac{\mathrm{Re\ Pr}\ \Delta x^2}{6}.
\end{aligned} \tag{12}$$

3.1. Fast pressure-correction method

To advance the momentum equation in time, we develop FastP*PC, a pressure-correction methodology for flows with phase change, which is an extension of the FastP* method [26,30]. The advantage of this approach is that it reduces the Poisson equation that must be solved at each time step from variable- to constant-coefficient. Therefore, a direct, FFT-based Poisson solver can be used, which, in our experience, is at least ten times faster than iterative methods such as multigrid.

Eq. (3) is first written in a more compact form as

$$\frac{\partial \mathbf{u}}{\partial t} = -\frac{1}{\rho}\nabla p + \mathbf{RU}. \tag{13}$$

We compute an approximate velocity field, $\mathbf{u}^*$, by neglecting the pressure gradient in Eq. (13) and integrating in time using the second-order Adams-Bashforth scheme

$$\frac{\mathbf{u}^* - \mathbf{u}^n}{\Delta t} = \frac{3}{2}\mathbf{RU}^n - \frac{1}{2}\mathbf{RU}^{n-1}, \tag{14}$$

where

$$\mathbf{RU}^n = -\mathbf{u}_m^n\cdot\nabla\mathbf{u}_m^n + \frac{1}{\rho^{n+1}}\left\{\frac{1}{\mathrm{Re}}\nabla\cdot\left[\mu^{n+1}\left(\nabla\mathbf{u}_m^n + (\nabla\mathbf{u}_m^n)^T\right)\right] + \left[\frac{1}{\mathrm{We}}\kappa^{n+1} + \left(\frac{\dot{m}''}{\mathrm{Re\ Sc}}\right)^2\left(\frac{1}{\rho_g}-\frac{1}{\rho_l}\right)\right]\nabla H^{n+1}\right\}, \tag{15}$$

where the relationship $\delta_\Sigma\mathbf{n} = \nabla H$ is used. The method for approximating the Heaviside step function, H, will be discussed later in this section.

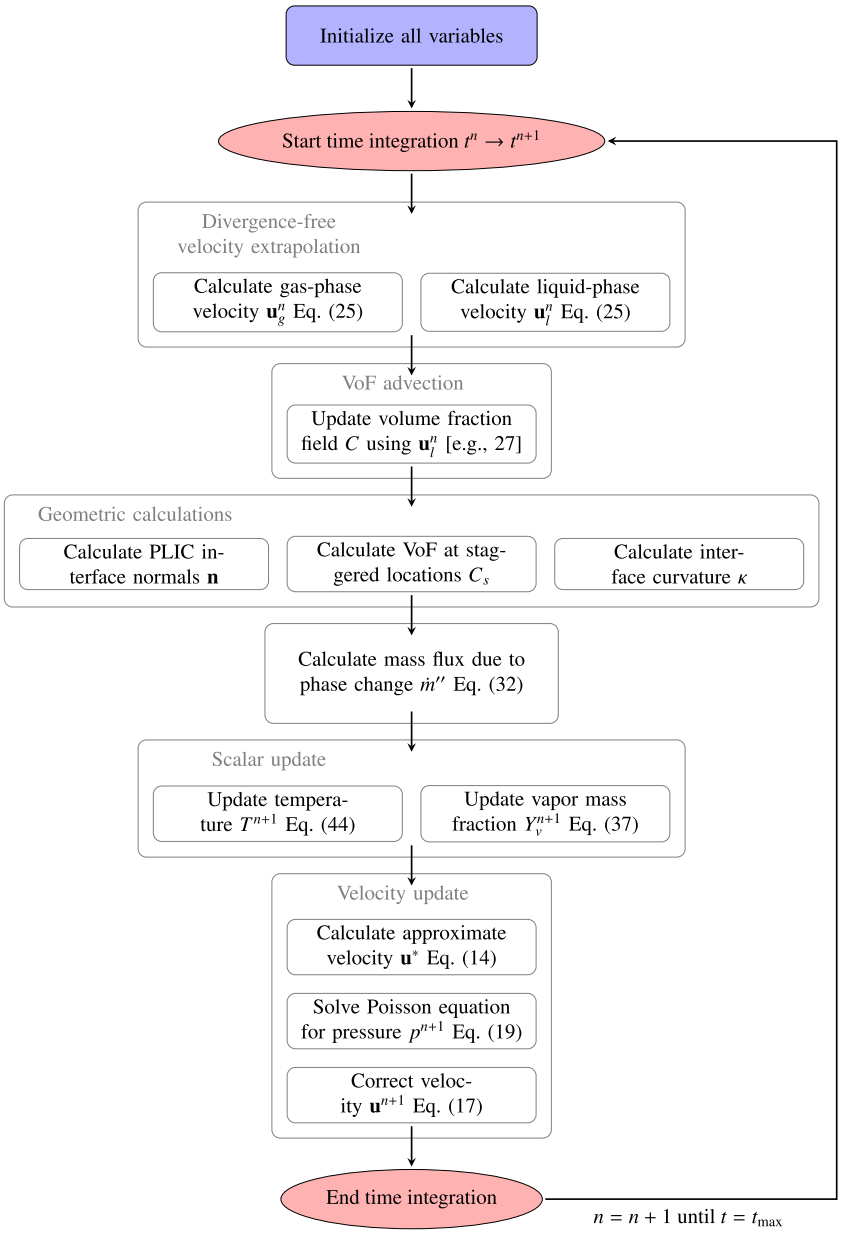

Fig. 3. Flowchart of flow solver for simulating incompressible gas-liquid flows with phase change using the volume-of-fluid method and pressure-correction method (FastP*PC).

We also introduce the phase-wise extended velocity field $\mathbf{u}_m$ for the liquid ($m = l$) and gas ($m = g$). These velocity fields ($\mathbf{u}_m$) are computed using the methodology that is described in Section 3.3. Because the momentum equation Eq. (3) is discretized using the central difference scheme for all computational cells, and therefore the finite-difference stencil overlaps liquid and gas velocity components in the vicinity of the interface, $\mathbf{u}_m$ is required to compute the numerical fluxes **RU**. For example, if left untreated, it can be noted from Eq. (3), that the presence of a velocity jump, $[\![\mathbf{u}]\!]$, in the viscous term would lead to an artificial pressure spike at the interface that scales as

$$p_{[\![\mathbf{u}]\!]} \propto \frac{[\![\mu \mathbf{u} \cdot \mathbf{n}]\!]}{h}, \tag{16}$$

as shown by the numerical results in Section 4.1.1.

To decide whether $\mathbf{u}_l$ or $\mathbf{u}_g$ is used for a given computational cell when computing **RU**, we compute the volume fraction of liquid at the staggered locations (e.g. $x_{i+1/2,j}$) and denote this field as C_s as previously done in [30,31]. Fig. 4 depicts how C_s is defined and calculated. To calculate $C_{s,i+1/2,j}$ (see Fig. 4(a)), we define a control volume of side length h (denoted by the dashed line), centered at

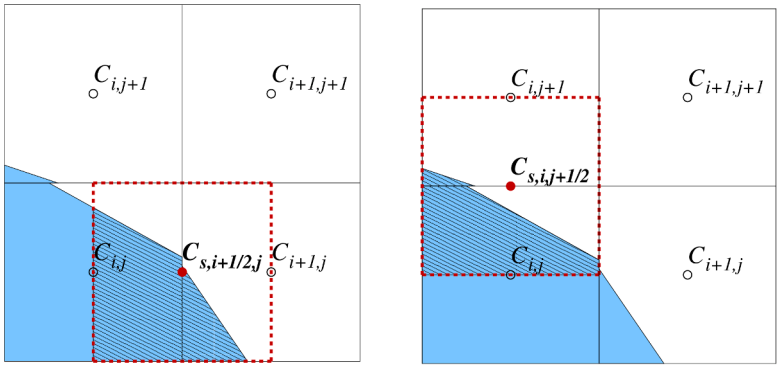

(a) Control volume for calculating $C_{s,i+1/2,j}$ (b) Control volume for calculating $C_{s,i,j+1/2}$

Fig. 4. Illustration of how the liquid volume fraction at staggered locations (C_s) is calculated. The control volumes for the volume calculation are indicated by the red dashed lines. Volume that is included in $C_{s,i+1/2,j}$ and $C_{s,i,j+1/2}$ is indicated by the hatched regions.

$x_{i+1/2,j}$. We then calculate the area (volume in 3D) cut by the PLIC interface in the left half and the right half (denoted by hatches), and sum these contributions to get $C_{s,i+1/2,j}$. An analogous procedure is used to calculate $C_{s,i,j+1/2}$ (Fig. 4(b)). In our solver, these operations are performed with the analytical tools of López and Hernández [32]. If $C_s < 0.5$ in a computational cell, then $\mathbf{u}_g$ is used to compute **RU** in Eq. (3), else $\mathbf{u}_l$ is used. The staggered volume fraction field C_s will prove to be useful in other portions of the solution algorithm.

The final velocity at the new time step, $\mathbf{u}^{n+1}$, is obtained in the pressure-correction (projection) step

$$\frac{\mathbf{u}^{n+1}-\mathbf{u}^{*}}{\Delta t} = -\left[\frac{1}{\rho_0}\nabla p^{n+1} + \left(\frac{1}{\rho^{n+1}} - \frac{1}{\rho_0}\right)\nabla \hat{p}\right], \tag{17}$$

where, as in [26], the pressure gradient is split into a constant-coefficient part ($1/\rho_0$) and variable-coefficient part ($1/\rho^{n+1}$) [33], where the constant-coefficient part is treated implicitly and the variable-coefficient part explicitly as

$$\frac{1}{\rho^{n+1}}\nabla p^{n+1} \rightarrow \frac{1}{\rho_0}\nabla p^{n+1} + \left(\frac{1}{\rho^{n+1}} - \frac{1}{\rho_0}\right)\nabla \hat{p}, \tag{18}$$

where $\rho_0 = \min(\rho^{n+1})$ for numerical stability and $\hat{p}$ is a second-order explicit approximation of p^{n+1}, i.e. $\hat{p} = 2p^n - p^{n-1}$. The pressure at the new time step, p^{n+1}, is obtained by solving the Poisson equation for pressure

$$\nabla^2 p^{n+1} = \nabla\cdot\left[\left(1-\frac{\rho_0}{\rho^{n+1}}\right)\nabla\hat{p}\right] + \frac{\rho_0}{\Delta t}\left(\nabla\cdot\mathbf{u}^{*} - \nabla\cdot\mathbf{u}^{n+1}\right), \tag{19}$$

where $\nabla\cdot\mathbf{u}^{n+1}$ is given by

$$\nabla\cdot\mathbf{u}^{n+1} = \frac{1}{\mathrm{Re}\,\mathrm{Sc}}\dot{m}''^{(n+1)}\left(\frac{1}{\rho_g^{n+1}} - \frac{1}{\rho_l^{n+1}}\right)\|\nabla H^{n+1}\|, \tag{20}$$

where we have used $\delta_\Sigma = \|\nabla H\|$. The Heaviside step function H is approximated using the continuum surface force (CSF) approach [34] such that H is replaced by the volume fraction C. The resulting 2D CSF discretization of δ_Σ at cell centers is

$$\|\nabla C\|_{i,j} = \sqrt{\left(\frac{C_{i+1,j}-C_{i-1,j}}{2h}\right)^2 + \left(\frac{C_{i,j+1}-C_{i,j-1}}{2h}\right)^2}. \tag{21}$$

Because $\nabla\cdot\mathbf{u}$ is located at cell centers, Eq. (21) would need to be used in Eq. (20). This leads to relatively large smearing of the velocity jump over a characteristic thickness $2h$. Here we propose a new discretization that reduces the velocity jump thickness from $2h$ to h, by using the staggered volume fraction field.

Using C_s, the resulting two-dimensional discretization of δ_Σ at cell-centered locations is

$$\|\nabla C_s\|_{i,j} = \sqrt{\left(\frac{C_{s,i+1/2,j}-C_{s,i-1/2,j}}{h}\right)^2 + \left(\frac{C_{s,i,j+1/2}-C_{s,i,j-1/2}}{h}\right)^2}. \tag{22}$$

Fig. 5 shows contours of $\|\nabla C\|_{i,j}$ and $\|\nabla C_s\|_{i,j}$ around a circular droplet. To summarize, our spatial discretization of Eq. (20) is

$$\frac{u_{i+1/2,j}-u_{i-1/2,j}}{h} + \frac{v_{i,j+1/2}-v_{i,j-1/2}}{h} = \frac{1}{\mathrm{Re}\,\mathrm{Sc}}\left(\frac{1}{\rho_g}-\frac{1}{\rho_l}\right)\dot{m}''\sqrt{\left(\frac{C_{s,i+1/2,j}-C_{s,i-1/2,j}}{h}\right)^2 + \left(\frac{C_{s,i,j+1/2}-C_{s,i,j-1/2}}{h}\right)^2}. \tag{23}$$

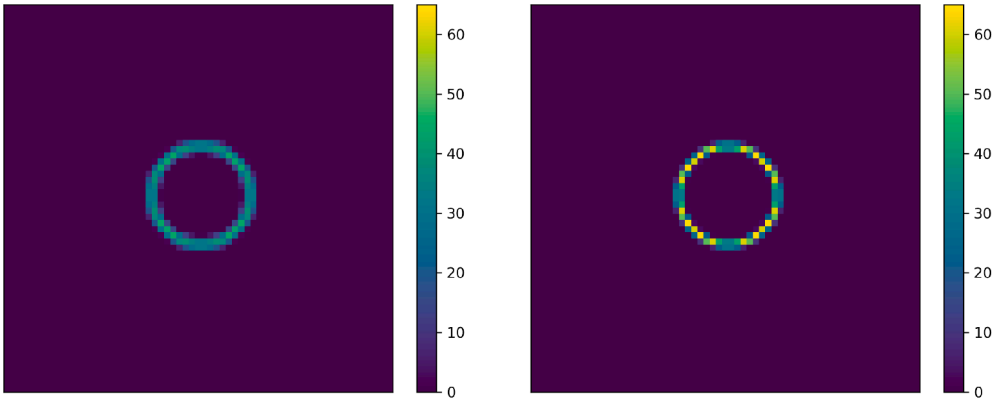

(a) $\|\nabla C\|_{i,j}$ (b) $\|\nabla C_s\|_{i,j}$

Fig. 5. Contours of the two-dimensional discretization of δ_Σ illustrating the difference between using the (a) cell-centered discretization C and (b) staggered discretization C_s.

3.2. VoF advection in the presence of phase change

Our VoF scheme in the presence of phase change proceeds by advecting the Heaviside step function, H, using the velocity of the reference phase ($H = 1$), i.e. the liquid-phase velocity, $\mathbf{u}_l$, and includes a source term to account for phase change as

$$\frac{\partial H}{\partial t} + \mathbf{u}_l \cdot \nabla H = -\frac{1}{\mathrm{Re\,Sc}} \frac{\dot{m}''}{\rho_l} \delta_\Sigma. \tag{24}$$

From Eq. (1), it is clear that the "one-fluid" velocity field, $\mathbf{u}$, is not solenoidal in cells containing the interface. A necessary condition for Eq. (24) to conserve mass in discretized form is that the liquid velocity must be divergence-free in discretized form ($\nabla \cdot \mathbf{u}_l = 0$) including computational cells containing the liquid-gas interface. In the next section, we will describe how the liquid velocity field extension is computed for computing the divergence-free $\mathbf{u}_l$ field used in Eq. (24).

3.3. Divergence-free velocity extrapolation

In this section, we describe the method for extending the divergence-free gas- and liquid-phase velocities, $\mathbf{u}_g$ and $\mathbf{u}_l$, in the cells across the interface, i.e. where $||\nabla C_s|| > 0$ (see Fig. 6 for $\mathbf{u}_l$). These extended velocity fields are needed for two purposes: first, to properly compute numerical fluxes in mixed liquid/gas cells as explained in Section 3.1 and, second, an extended divergence-free liquid velocity field is needed for the VoF advection scheme as described in Section 3.2 to capture the motion of the interface properly in the presence of phase change. A similar method was used to determine velocity boundary conditions for free surface fluid flows by [35]. Previous velocity extension methods project the liquid velocity field to a divergence-free space. This has the unphysical side effect of modifying the entire liquid velocity field after solving the conservation equations. The present method modifies only the extended velocities while preserving the velocity field within the liquid or gas (depending on the direction of the extension).

The method for extending the liquid-phase velocity (identical steps are used to extend the gas-phase velocity by interchanging the subscripts l and g in what follows) starts with solving an equation for the extended liquid velocity that: 1. is applied locally where

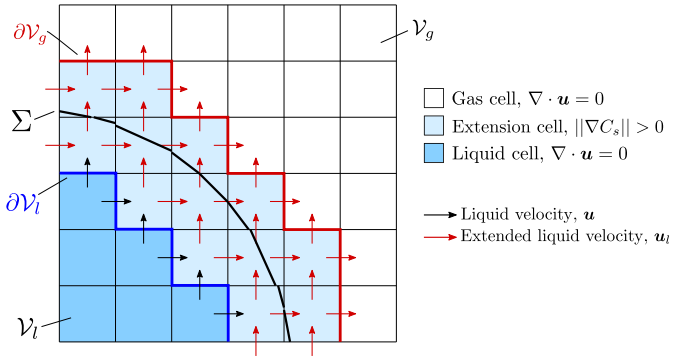

Fig. 6. Illustration of the discretization employed in the divergence-free extrapolation methodology.

the one-fluid velocity divergence is non-zero, i.e., light-blue cells in Fig. 6; 2. provides as its solution an extended liquid velocity, i.e., red arrows in Fig. 6, with zero divergence; 3. satisfies the BC's for liquid velocity on the liquid side and zero-divergence on the gas side, i.e., solid blue line and solid red line, respectively, in Fig. 6. In order to satisfy these three conditions, and inspired by the work in astrophysics to extrapolate magnetic fields such that the resulting field satisfies Gauss' law [36], in the cells where the divergence of the one-fluid velocity is non zero, we write the following equation,

$$\nabla(\nabla \cdot \mathbf{u}_l) = 0, \tag{25}$$

and boundary conditions,

$$\begin{aligned} \mathbf{u}_l|_{\partial \mathcal{V}_l} &= \mathbf{u}(\mathbf{x}, t) \\ \nabla \cdot \mathbf{u}_l|_{\partial \mathcal{V}_g} &= 0, \end{aligned} \tag{26}$$

where $\partial \mathcal{V}_l$ is the surface of the interface on the liquid side from which the extension originates (blue line in Fig. 6) and $\partial \mathcal{V}_g$ is the surface of the interface on the gas side where the extension terminates (red line in Fig. 6). $\partial \mathcal{V}_l$ is defined as the intersection of computational cells where $C = 1$ and $||\nabla C_s|| > 0$, and $\partial \mathcal{V}_g$ is defined as the intersection of computational cells where $C = 0$ and $||\nabla C_s|| > 0$. Fig. 6 also depicts the liquid velocity $\mathbf{u}$ and the extended liquid velocity $\mathbf{u}_l$ used for the discretization of Eq. (25) and where the boundary conditions, Eq. (26), are imposed in the vicinity of the liquid-gas interface. Eq. (25) imposes a zero gradient to the velocity divergence of the extended liquid velocity, and the BCs expressed in Eq. (26) leave $\mathbf{u}_l$ unchanged on the liquid side, and impose zero divergence on the extended side in the gas phase. Thus, the solution of Eq. (25) with the BCs of Eq. (26) yields a solution for $\mathbf{u}_l$ that satisfies $\nabla \cdot \mathbf{u}_l = 0$ throughout the light blue region.

We discretize Eq. (25) using the second-order central difference scheme on a staggered Cartesian uniform mesh. For brevity, we report the spatial discretization in 2D for the u- and v-components of velocity. The extension to 3D and the w component follows analogously from the 2D discretization. In 2D, the $x-$ and $y-$components of Eq. (25) are discretized, respectively, as

$$\left(\nabla \cdot \mathbf{u}_l\right)_{i+1,j} - \left(\nabla \cdot \mathbf{u}_l\right)_{i,j} = 0, \tag{27}$$

and

$$\left(\nabla \cdot \mathbf{u}_l\right)_{i,j+1} - \left(\nabla \cdot \mathbf{u}_l\right)_{i,j} = 0, \tag{28}$$

where $\left(\nabla \cdot \mathbf{u}_l\right)_{i,j}$ is computed at the center of the (i, j) cell. Then, using the second-order central discretization for the velocity divergence in the equations above, and solving Eq. (27) for the staggered liquid velocity in the $x-$direction, $(u_l)_{i+1/2,j}$, yields

$$(u_l)_{i+1/2,j} = \frac{1}{2}\left[(u_l)_{i+3/2,j} + (u_l)_{i-1/2,j} + (v_l)_{i+1,j+1/2} + (v_l)_{i,j-1/2} - (v_l)_{i+1,j-1/2} - (v_l)_{i,j+1/2}\right], \tag{29}$$

and, solving Eq. (28) for the staggered liquid velocity in the $y-$direction, $(v_l)_{i,j+1/2}$, yields

$$(v_l)_{i,j+1/2} = \frac{1}{2}\left[(v_l)_{i,j+3/2} + (v_l)_{i,j-1/2} + (u_l)_{i+1/2,j+1} + (u_l)_{i-1/2,j} - (u_l)_{i-1/2,j+1} - (u_l)_{i+1/2,j}\right]. \tag{30}$$

The velocity extension algorithm begins by determining and storing the indices of velocities that must be extrapolated (red arrows in Fig. 6). The velocities with these stored indices are then updated iteratively using Eqs. (29) and (30) in conjunction with the pointwise Jacobi over-relaxation (JOR) method with a relaxation factor $\omega = 0.32$. The initial guess for $\mathbf{u}_l$ to start the iterations of JOR is the one-fluid velocity field, $\mathbf{u}$. At the end of each iteration, we compute the velocity divergence at every extension cell (light-blue cells in Fig. 6), and we calculate the mean magnitude of the velocity divergence. The iterative solver proceeds until this mean falls below a specified tolerance. The VoF method's mass conservation accuracy depends on the liquid velocity field's discrete divergence-free condition. A solver tolerance of 10^{-15} could theoretically achieve near-machine-precision mass conservation, but we use 10^{-10} for efficiency, yielding a 10^{-10} mass conservation error. This error is unrelated to numerical instabilities. JOR was chosen for ease of implementation, but the use of more efficient linear equation solvers is pursuable. It is important to note that Eq. (25) is only solved in a narrow region of width $2h$ where $\nabla \cdot \mathbf{u} \neq 0$, such that the computational cost scales with the surface area of the liquid phase. For example, if we consider DNS of droplet-laden isotropic turbulence [37] with a droplet volume fraction of 5%, the number of unknowns in Eq. (25) would be 1.9% of the total number of grid points, therefore, this velocity extension step represents a very small percentage of the total computational cost.

3.4. Computation of mass flux due to phase change

In this section we describe how to calculate the mass flow rate per unit area due to phase change Eq. (2) in cells containing the interface ($0 < C < 1$). Instead of computing the gradient of Y_v and taking the normal projection as shown in Eq. (2), we compute the normal derivative directly as

$$\dot{m}'' = \frac{\rho_g}{1 - Y_v}\frac{\partial Y_v}{\partial n}, \tag{31}$$

using the normal probe approach similar to that of [38]. Consider Fig. 7 in which we have illustrated a typical computational cell in which $\dot{m}''$ must be computed. The first point is located at the centroid of the PLIC interface, $Y_{v,sat}$. From the $Y_{v,sat}$ location, two

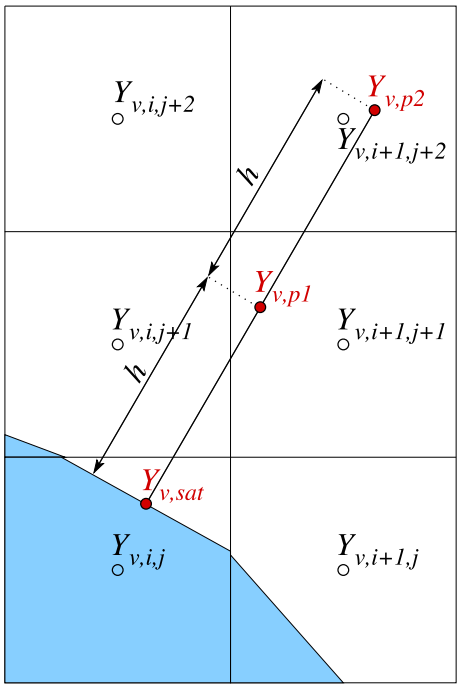

Fig. 7. Computational stencil for obtaining the normal gradient of Y_v, $\partial Y_v/\partial n$, in cells containing the gas-liquid interface. The first red point is located at the PLIC centroid and is at saturation conditions ($Y_{v,sat}$) and the two other red points, $Y_{v,p1}$ and $Y_{v,p2}$, are located in the gas phase at a distance h and $2h$, respectively, from the interface in the normal direction. The values of $Y_{v,p1}$ and $Y_{v,p2}$ are calculated at the determined locations using Lagrange interpolating polynomials from the known values of $Y_{v,i,j}$ at the cell centers (empty circles).

virtual probes, $Y_{v,p1}$ and $Y_{v,p2}$, are extended into the gas phase in the direction normal to the interface at a distance equal to h and $2h$, respectively. Using the normal probe values, Eq. (31) is discretized using a one-sided second-order finite difference scheme

$$\dot{m}''^{n+1}_{i,j} = \frac{\rho^{n+1}}{1 - Y^n_{v,sat}} \frac{3Y^n_{v,sat} - 4Y^n_{v,p1} + Y^n_{v,p2}}{2h}. \tag{32}$$

The vapor mass fraction at the probe locations is computed using three-dimensional Lagrange interpolation. A second degree (quadratic) Lagrange interpolating polynomial is constructed by using the values of Y_v in the nearest nine grid (twenty-seven) nodes of $Y_{v,p1}$ in 2D (3D).

As previously mentioned, saturation conditions are assumed at the interface. Therefore, $Y_{v,sat}$ is a function of the saturation pressure, p_{sat}, which is found using the Clausius-Clapeyron relation

$$\tilde{p}_{\text{sat}} = \tilde{p}_{\text{boil}} \exp\left[-\frac{\Delta\tilde{h}_v \tilde{M}_v}{\tilde{R}_u}\left(\frac{1}{\tilde{T}_{\text{sat}}} - \frac{1}{\tilde{T}_{\text{boil}}}\right)\right], \tag{33}$$

where $\tilde{p}_{\text{boil}}$ is the vapor pressure at the boiling temperature $\tilde{T}_{\text{boil}}$, $\tilde{M}_v$ is the molar mass of the vapor, and $\tilde{T}_{\text{sat}}$ is the saturation temperature. The non-dimensional form of Eq. (33) is

$$p_{\text{sat}} = \exp\left[-\frac{1}{\text{Ste}_c}\left(\frac{1}{T_{\text{sat}}} - \frac{1}{T_{\text{boil}}}\right)\right], \tag{34}$$

where $\tilde{p}_{\text{boil}}$ and $\tilde{T}_g$, the initial ambient gas temperature, have been used as reference values for the non-dimensionalization, and where we have introduced a pseudo Stefan number defined as

$$\text{Ste}_c = \frac{\tilde{R}_u \tilde{T}_g}{\Delta\tilde{h}_v \tilde{M}_v}, \tag{35}$$

where $\tilde{R}_u$ is the universal gas constant. Note that the saturation temperature T_{sat} is calculated at the PLIC centroid in each cell. Because the PLIC centroid is off-grid, we use linear interpolation to approximate T_{sat} from the neighboring cell centered values of T. The mass fraction of saturated vapor at the gas-liquid interface is

$$Y_{v,\text{sat}} = \frac{p_{\text{sat}} \frac{M_v}{M_a}}{p_{\text{sat}} \frac{M_v}{M_a} + (1 - p_{\text{sat}})}, \tag{36}$$

where M_v/M_a is the molar mass ratio of the liquid vapor and ambient gas.

As a final step, we must populate cells adjacent to the interface where $\|\nabla C_s\|_{i,j} > 0$ with an estimate of $\dot{m}''$. This is done by taking the arithmetic mean of the non-zero values of $\dot{m}''$ in the eight (twenty-six) neighboring cells in 2D (3D).

3.5. Computation of the vapor mass fraction

The vapor mass fraction at the new time step, Y_v^{n+1}, is computed by integrating Eq. (6) in time using the first-order Euler scheme

$$\frac{Y_v^{n+1} - Y_v^n}{\Delta t} = RY^n, \tag{37}$$

where

$$RY^n = -(\mathbf{u}_g^n \cdot \nabla)Y_v + \frac{1}{\mathrm{Re\,Sc}}\nabla^2 Y_v^n. \tag{38}$$

A first-order explicit scheme is chosen in Eq. (37) for two reasons: (i) the time integration of the VoF field is first-order accurate, and therefore using a higher-order time integration for Y_v would not increase the global accuracy, and (ii) the interface may, in general, cross into new computational cells, where the fluxes of Y_v at $t = t^{n-1}$ are unavailable. If a second-order linear multistep method like Adams-Bashforth were adopted, it would need to switch to first-order for such events. When computing RY^n, if the finite difference stencil crosses into the liquid phase where there is no vapor, we switch to a one-sided finite difference stencil that is directed into the gas phase, i.e. only use values of $Y_{v,i,j}$ in cells with $C_{i,j} < 0.5$. Our one-sided discretization will now be described in more detail.

The Dirichlet boundary condition $Y_v(x = \Sigma) = Y_{v,sat}$ requires that the spatial derivatives in Eq. (38) be calculated on a non-uniform grid because, in general, the interface does not coincide with the grid. Consider, for example, a one-dimensional case in which the interface is located between x_{i-1} and x_i as depicted in Fig. 8. The interface is located a distance θh from x_i and $(1-\theta)h$ from x_{i-1}, where h is the grid spacing and θ is the distance from the interface to x_i normalized to the range [0,1]. The procedure for calculating θ will be described later in this section. The m-th derivative of Y_v at x_i is then calculated as

$$\left.\frac{\partial^m Y_v}{\partial x^m}\right|_{x=x_i} = \gamma_{i,0}^m Y_{v,sat} + \gamma_{i,1}^m Y_{v,i} + \gamma_{i,2}^m Y_{v,i+1} + \gamma_{i,3}^m Y_{v,i+2} + \gamma_{i,4}^m Y_{v,i+3} \tag{39}$$

on the stencil $x = x_i + [-\theta h, 0, h, 2h, 3h]$, with the derivative being calculated at $x = x_i$. The finite difference weights $\gamma_{i,n}^m$ for the m-th derivative are calculated using the method described in [39]. In general, this scheme is at least fourth-order accurate for the first derivative and third-order accurate for the second derivative. Special care must be taken when $\theta << 1$ since in the limit $\theta \to 0$ some of the γ_i coefficients go to infinity. Therefore, we limit use of Eq. (39) to $\theta \geq 1/4$. If $\theta < 1/4$, we omit $Y_{v,i}$ and the derivatives are calculated as

$$\left.\frac{\partial^m Y_v}{\partial x^m}\right|_{x=x_i} = \gamma_{i,0}^m Y_{v,sat} + \gamma_{i,1}^m Y_{v,i+1} + \gamma_{i,2}^m Y_{v,i+2} + \gamma_{i,3}^m Y_{v,i+3}. \tag{40}$$

on the stencil $x = x_i + [-\theta h, h, 2h, 3h]$ with the derivative evaluated at $x = x_i$. Eq. (40) is at least third-order accurate for the first derivative and second-order accurate for the second derivative. The extension of the above described 1D discretization to multidimensions is straightforward, and therefore has been left to the reader. The results in Section 4 correspond to the full 3D implementation.

We now address the problem of determining θ. Unlike level-set methods where a signed distance function to the interface is tracked, VoF methods do not inherently contain this information. One possible solution is to use the height-function technique, e.g. [40]. However, we propose a novel solution for this particular problem. The idea is to use knowledge of the volume of liquid in control volumes centered at staggered locations C_s. From this staggered volume fraction field, one can estimate the distance between the interface and cell centers $x_{i,j}$. If we consider the example from Fig. 8 of the interface located between x_{i-1} and x_i, θ is computed as

$$\theta = 1 - C_{s,i-1/2}, \tag{41}$$

where this computation is exact for cases where one half of the staggered control volume is fully liquid, and the interface intersects only with the lateral sides of the second half of the staggered control volume.

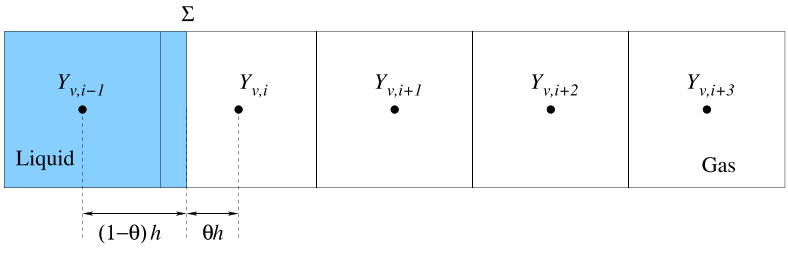

Fig. 8. Computation of Y_v derivatives at the interface with Dirichlet boundary condition $Y_{v,sat}$.

For example, in the $2D$ configuration shown in Fig. 4(a), the interface is located between $\mathbf{x}_{i,j}$ and $\mathbf{x}_{i+1,j}$, therefore, to calculate $\partial_x Y_v$ at $\mathbf{x}_{i+1,j}$, one would use

$$\theta_x = 1 - C_{s,i+1/2,j}, \tag{42}$$

where θ_x is the distance between the interface and $\mathbf{x}_{i+1,j}$, and the resulting finite-difference stencil would be $x = x_{i+1} + [-\theta_x h, 0, h, \ldots]$ if $\theta_x \geq 1/4$ or $x = x_{i+1} + [-\theta_x h, h, 2h, \ldots]$ if $\theta_x < 1/4$. Considering Fig. 4(b) as our next example, the interface is located between $\mathbf{x}_{i,j}$ and $\mathbf{x}_{i,j+1}$, therefore, to calculate $\partial_y Y_v$ at $\mathbf{x}_{i,j+1}$, one would use

$$\theta_y = 1 - C_{s,i,j+1/2}, \tag{43}$$

where θ_y is the distance between the interface and $\mathbf{x}_{i,j+1}$, and the resulting finite-difference stencil would be $y = y_{j+1} + [-\theta_y h, 0, h, \ldots]$ if $\theta_y \geq 1/4$ or $y = y_{j+1} + [-\theta_y h, h, 2h, \ldots]$ if $\theta_y < 1/4$.

3.6. Computation of the temperature

The temperature at the new time step, T^{n+1}, is found by integrating Eq. (5) in time using the second-order Adams-Bashforth scheme

$$\frac{T^{n+1} - T^n}{\Delta t} = \frac{3}{2} RT^n - \frac{1}{2} RT^{n-1}, \tag{44}$$

where

$$RT^n = RCT^n + RDT^n + RST^n, \tag{45}$$

where RCT^n, RDT^n, and RST^n are, respectively, the convective, diffusive, and source terms on the right-hand side of the energy Eq. (5) at time t^n, defined as

$$\begin{aligned} RCT^n &= -\mathbf{u}_m^n \cdot \nabla T^n \\ RDT^n &= \frac{1}{\rho^{n+1} c_p^{n+1}} \frac{1}{\mathrm{RePr}} \left[\nabla \cdot (k^n \nabla T^n)\right] \\ RST^n &= -\frac{1}{\rho^{n+1} c_p^{n+1}} \frac{1}{\mathrm{Ste}} \dot{m}^n \|\nabla C_s^n\|. \end{aligned} \tag{46}$$

We discretize the terms in Eq. (46) using second-order central differences. The discretization of RCT^n is standard and equivalent to what is done in single-phase flow. We present a novel discretization of RDT^n and RST^n here in 2D. RDT^n is discretized as follows (where we omit the time level n)

$$\begin{aligned} RDT_{i,j} = \frac{1}{\rho_{i,j} c_{p,i,j}} \frac{1}{\mathrm{RePr}} \Bigg[&\frac{k_{i+1/2,j}(T_{i+1,j} - T_{i,j}) - k_{i-1/2,j}(T_{i,j} - T_{i-1,j})}{h^2} + \\ &\frac{k_{i,j+1/2}(T_{i,j+1} - T_{i,j}) - k_{i,j-1/2}(T_{i,j} - T_{i,j-1})}{h^2} \Bigg], \end{aligned} \tag{47}$$

where $\rho_{i,j} c_{p,i,j}$ is calculated using the arithmetic mean

$$\rho_{i,j} c_{p,i,j} = \rho_l c_{p,l} C_{i,j} + \rho_g c_{p,g} (1 - C_{i,j}). \tag{48}$$

To calculate the staggered thermal conductivities in Eq. (47), we leverage the staggered volume fraction field C_s as

$$\begin{aligned} k_{i+1/2,j} &= k_l C_{s,i+1/2,j} + k_g (1 - C_{s,i+1/2,j}) \\ k_{i,j+1/2} &= k_l C_{s,i,j+1/2} + k_g (1 - C_{s,i,j+1/2}). \end{aligned} \tag{49}$$

Compared to using the standard practice of taking the arithmetic mean of cell centered transport properties to obtain face centered properties, i.e. $k_{i+1/2,j} = \frac{1}{2}(k_{i+1,j} + k_{i,j})$, Eq. (49) leads to a sharper representation of the discontinuity in the temperature gradient near the interface because the thermal conductivity transitions between k_l and k_g over a distance h instead of $2h$.

RST^n is discretized as follows

$$RST_{i,j} = -\frac{1}{\rho_{i,j} c_{p,i,j}} \frac{1}{\mathrm{Re\,Sc\,Ste}} \dot{m}_{i,j}^n \left[\left(\frac{C_{s,i+1/2,j} - C_{s,i-1/2,j}}{h} \right)^2 + \left(\frac{C_{s,i,j+1/2} - C_{s,i,j-1/2}}{h} \right)^2 \right]^{1/2}. \tag{50}$$

Note that using the staggered volume fractions to discretize the regularized Dirac δ function in Eq. (46) as shown in Eq. (50) leads to less numerical smearing of the source term in Eq. (5).

4. Results

The numerical method presented in Section 3 is implemented in a 3D flow solver. We consider several 1D, 2D, and 3D test problems to verify and validate the flow simulations. We first verify the VoF advection scheme in the presence of phase change that was presented in Section 3.2 by simulating a 1D evaporating pool and 2D evaporating and condensing droplets with a constant

evaporative mass flux, $\dot{m}''$, for which analytical solutions are available. This case is also used to demonstrate the divergence-free extrapolation methodology presented in Section 3.3. Second, we verify the computation of the vapor mass flux presented in Section 3.4 and report the computed order of accuracy. Next, a 1D Stefan flow is considered with a stationary interface for which we have derived an analytical solution for the temperature and vapor mass fraction profile. This case is used to test the discretization of the vapor mass-fraction and energy equations, Eqs. (6) and (5), presented in Sections 3.5 and 3.6, respectively, in which the temperature and vapor-mass fraction fields are solved for. Finally, we verify the fully coupled 3D solver for an evaporating droplet in quiescent conditions and compare the results with the D^2-law.

4.1. Verification of VoF advection with constant mass flux

The objective of this section is to verify the accuracy of the method described in Section 3.2. We select test cases in which $\dot{m}''$ is set to a constant and the geometry of the gas-liquid interface is known exactly, allowing us to derive an analytical expression for the total volume of the liquid phase (VoF volume) as a function of time.

4.1.1. Evaporation of a liquid pool

We consider a 1D domain that contains one half gas and one half liquid separated by an interface as shown in Fig. 9. The lower boundary is a wall and the upper boundary is an outflow plane. The liquid remains at rest ($u_l = 0$) as the interface moves towards the wall. Using Eq. (9), it can be derived that the gas velocity is

$$u_g = \frac{1}{\mathrm{Re}\,\mathrm{Sc}}\dot{m}''\left(\frac{1}{\rho_g} - \frac{1}{\rho_l}\right). \tag{51}$$

The height of the interface is found starting from the mass balance equation at the interface Eq. (9). By integrating the interface velocity, u_Σ, we derive that the height of the interface evolves as

$$h(t) = h_0 - \frac{1}{\mathrm{Re}\,\mathrm{Sc}}\frac{\dot{m}''}{\rho_l}t, \tag{52}$$

where h_0 is the initial height.

For our test, we use a domain of length $L = 1$ discretized using 32 points, and the interface initialized at $h_0 = 0.5$. The non-dimensional parameters are $\mathrm{Re} = 200$, $\mathrm{Sc} = 1$, $\dot{m}'' = 30$, $\rho_l/\rho_g = 4$, and $\mu_l/\mu_g = 4$. The fluids are initially at rest.

Fig. 10 shows the time development of the interface height, $h(t)$, and the gas-phase velocity, $u_g(t)$. For both, there is excellent agreement between the exact and numerical solution. In fact, the solutions agree to machine precision. Something to notice is that $u_g(t)$ remains constant even as the interface crosses grid nodes. This demonstrates that imposing the velocity jump by discretizing the δ-function as Eq. (21) yields an exact balance of mass flux across the interface. Fig. 11(a) shows the presence of pressure spikes occurring near the interface at the first time step, and, which occur at every time-step, if the numerical fluxes Eq. (15) are calculated using the "one-fluid" velocity $\mathbf{u}$ instead of the phase-wise extended velocity $\mathbf{u}_m$ Fig. 11(b). We have tested other grid sizes and density ratios up to 10,000 and found that the solution agrees to machine precision for all cases.

4.1.2. Evaporation and condensation of a 2D droplet

We consider a 2D square domain with a wall on the left, right, and bottom boundary and an outflow on the top boundary. We initialize a circular droplet in the center of the domain and release it from rest in quiescent fluid. We impose a constant evaporative mass flux, $\dot{m}''$, such that Stefan flow is generated around the droplet. The Stefan flow propels the droplet away from (towards) the bottom wall in the case of evaporation (condensation). If the droplet remains circular (i.e. if the Weber number is sufficiently smaller than unity) then the normalized droplet diameter evolves in time as

$$\frac{D(t)}{D_0} = 1 - \frac{1}{\mathrm{Re}\,\mathrm{Sc}}\frac{2}{D_0}\frac{\dot{m}''}{\rho_l}t. \tag{53}$$

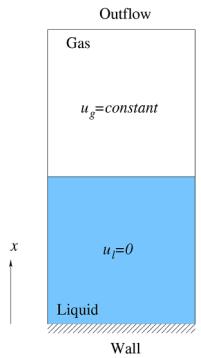

Fig. 9. Domain for 1D pool evaporation with constant $\dot{m}''$.

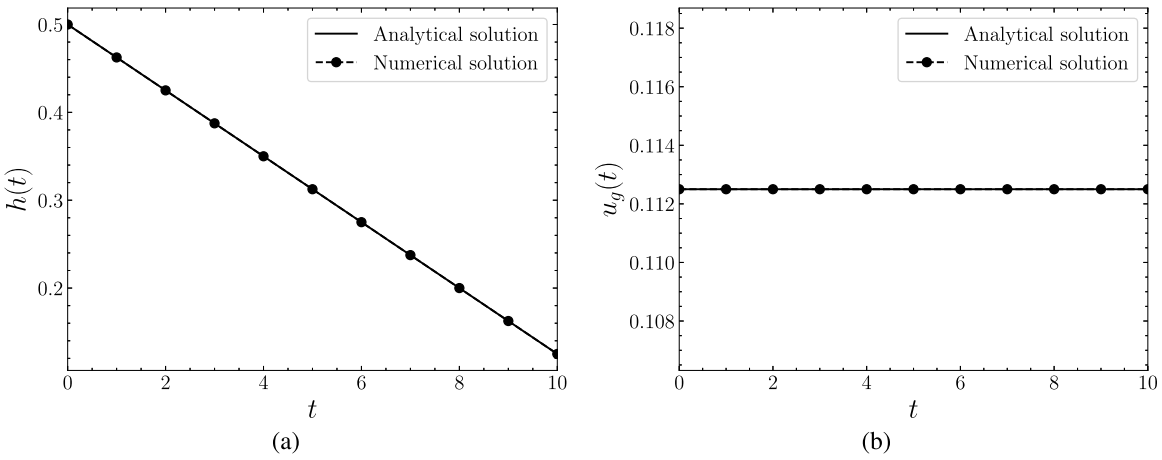

Fig. 10. Comparison of the numerical and analytical solutions for the time evolution of (a) the interface height $h(t)$, Eq. (52), and (b) the gas-phase velocity $u_g(t)$, Eq. (51), for the evaporation of the liquid pool problem (Fig. 9).

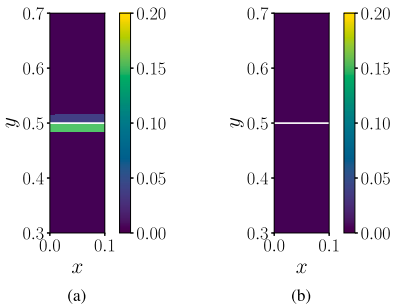

Fig. 11. Pressure contours at the first time step for the evaporation of the liquid pool problem (Fig. 9) illustrating the difference between computing the numerical fluxes **RU** with (a) the "one-fluid" velocity **u**, and (b) the phase-wise extended velocity $\mathbf{u}_m$. The white line is a $C = 0.5$ isocontour representing the gas-liquid interface.

For the test, we use a domain of length $L = 1$ discretized using 128^2 points. The initial droplet diameter is $D_0 = 0.25$. The non-dimensional parameters are Re = 50, Sc = 1, We = 1, $\dot{m}'' = 25$ for the evaporating droplet and $\dot{m}'' = -25$ for the condensing droplet, $\rho_l/\rho_g = 10$, 50 and 100, and $\mu_l/\mu_g = 1$, 5 and 10, respectively, such that $\nu_l/\nu_g = 0.1$ for all cases. Note that the droplet Weber number based on the initial gas phase velocity ($\mathrm{We}_D = \rho_g u_g^2 D/\sigma$, where u_g is given by Eq. (51)) varies from $\mathrm{We}_D = 0.05$ for $\rho_l/\rho_g = 10$ to $\mathrm{We}_D = 0.06$ for $\rho_l/\rho_g = 100$, and hence, $\mathrm{We}_D \ll 1$ which justifies the use of Eq. (53).

Fig. 12 shows the time development of $(D(t)/D_0)^2$ for the evaporating and condensing droplets at the various density ratios. In all cases, there is excellent agreement between the numerical and analytical solutions. These results demonstrate that the VoF advection algorithm for phase change presented in Section 3.2 is mass conserving. Table 2 shows the error in the mass ($E_m = |m_{\mathrm{sim}} - m_{\mathrm{exact}}|$) as function of the grid spacing Δx ($= 1/N$). m_{exact} is determined from the normalized droplet diameter in Eq. (53). The table shows that the mass is above second-order accurate.

Fig. 13 and 14 show the velocity vectors for the $\rho_l/\rho_g = 10$ cases at three different times ($t = 0$, 0.25, and 0.5). The figures show that our implementation of the $\nabla \cdot \mathbf{u}$ source/sink term in Eq. (1) leads to a sharp jump in the normal velocity at the interface as expected. Also, the Stefan flow generated by the evaporation or condensation process causes the droplet to be propelled away from or towards the wall, respectively. The droplet maintains a circular shape as it travels away from or towards the wall and while shrinking or growing in size. These figures demonstrate the ability of the VoF advection algorithm described in Section 3.2 to accurately capture evaporating and condensing droplets while in motion.

Table 2
Error in the mass as a function of the grid spacing Δx for an evaporating 2D droplet.

Δx	E_m	Rate
1/64	6.98e-4	–
1/128	7.07e-5	4.93
1/256	1.70e-5	2.08

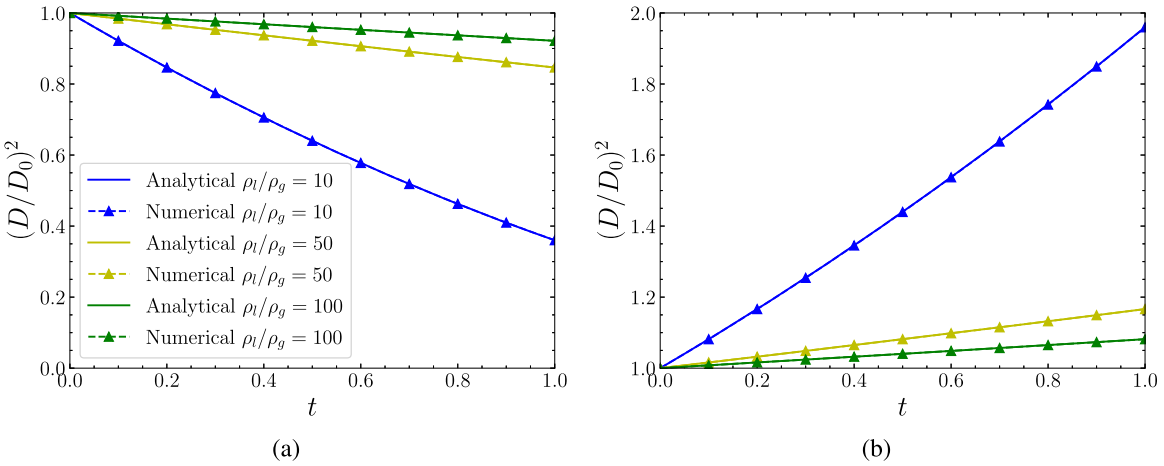

Fig. 12. Comparison of numerical and analytical solution, Eq. (53) of the time evolution of the normalized droplet diameter squared for (a) an evaporating 2D droplet and (b) condensing 2D droplet surrounded by three walls. The solutions are shown for density ratios of 10, 50, and 100.

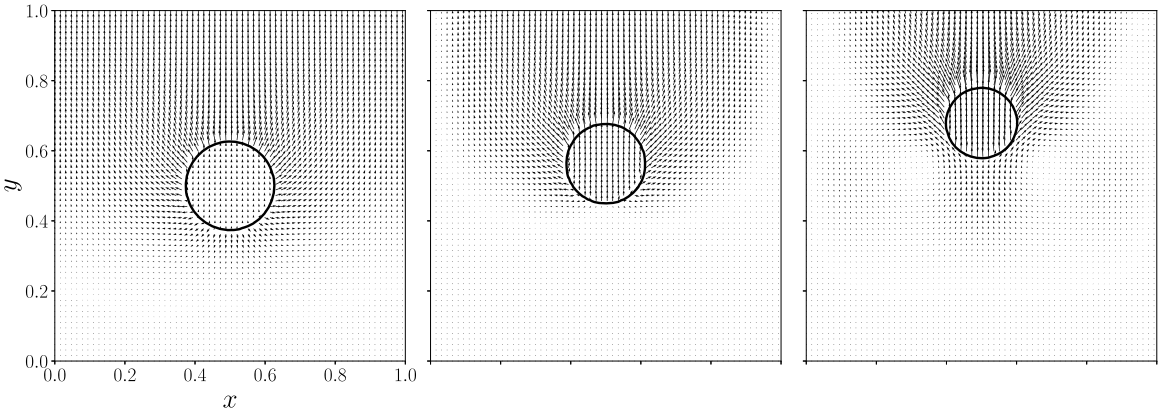

Fig. 13. Velocity vectors around the evaporating 2D droplet with $\rho_l/\rho_g = 10$ at $t = 0$, 0.25, and 0.5. The black line is a $C = 0.5$ isocontour representing the gas-liquid interface.

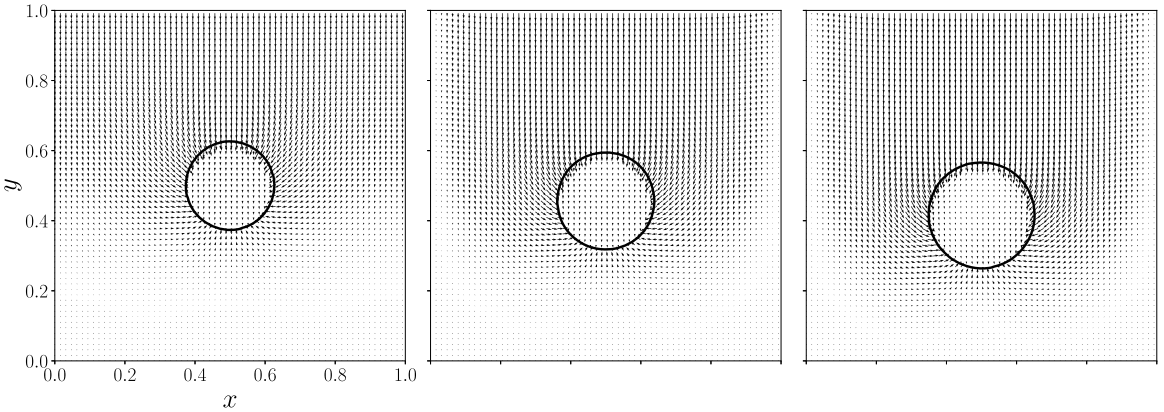

Fig. 14. Velocity vectors around the condensing 2D droplet with $\rho_l/\rho_g = 10$ at $t = 0$, 0.25, and 0.5. The black line is a $C = 0.5$ isocontour representing the gas-liquid interface.

Fig. 15 and 16 show a close-up of the velocity vectors and their respective divergence for the $\rho_l/\rho_g = 10$ cases at $t = 0$. The figures show the velocity field of the liquid and gas phase before and after the divergence-free extrapolation methodology described in Section 3.3. The figures show that, after extension, the velocity jump is effectively removed and the resulting velocity field satisfies $\nabla \cdot \mathbf{u} = 0$ both in the liquid and gas near the droplet surface. These figures demonstrate the ability of our novel divergence-free extrapolation technique described in Section 3.3 to accurately extend the velocity field in the liquid and gas phase and in the presence of evaporation and condensation.

4.2. Verification of mass flux computation

To verify the accuracy of the mass flux computation that was described in Section 3.4, we consider a 1D Stefan flow in the domain depicted in Fig. 9. We assume isothermal conditions and infinite Stefan number such that the energy equation can be neglected for this case. The vapor mass fraction field has Dirichlet boundary conditions applied at the gas-liquid interface and the outflow plane. We assume that $\rho_l/\rho_g = \infty$ such that the interface remains stationary ($\mathbf{u}_\Sigma = 0$) as the liquid evaporates (this can be deduced from Eq. (9)). Under these assumptions, we have derived analytical solutions for $Y_v(x)$ and $\dot{m}''$. In this section we only focus on $\dot{m}''$, and will return to verifying $Y_v(x)$ in the next section. The analytical mass flux is

$$\dot{m}''_{\text{exact}} = \frac{\rho_g}{L_g} \ln\left(\frac{1 - Y_{v,L}}{1 - Y_{v,sat}}\right), \tag{54}$$

where L_g is the distance from the interface to the outflow plane, and $Y_{v,L}$ and $Y_{v,sat}$ are the vapor mass fractions at the outflow plane and the interface, respectively.

The conditions for the test are $L_g = 0.5$, $\text{Re} = 200$, $\text{Sc} = 1$, $Y_{v,L} = 0$, $Y_{v,sat} = 0.5$, $\rho_l/\rho_g = \infty$, and $\mu_l/\mu_g = 4$. We initialize $Y_v = 0$ in the gas phase and then integrate in time until $Y_v(x)$ reaches the steady-state solution. When $Y_v(x)$ reaches steady-state, we compute $\dot{m}''$. We performed tests on three different grids, $N = 16$, 32, and 64. Table 3 shows the error in the mass flux ($E_{\dot{m}''} = |\dot{m}''_{\text{sim}} - \dot{m}''_{\text{exact}}|$) as function of the grid spacing Δx ($= 1/N$). The table shows that the mass flux calculation (Eq. (32)) is second-order accurate.

4.3. Verification of the vapor mass fraction and temperature fields

In this section we verify the accuracy of the methods for solving the vapor mass fraction and temperature fields as described in Sections 3.5 and 3.6. We consider the 1D Stefan flow problem illustrated in Fig. 17. Dirichlet conditions for vapor mass fraction and temperature are applied at the outflow boundary. At the lower wall, a Dirichlet boundary conditions is applied for temperature. At the interface, a Dirichlet boundary condition is applied for the saturated vapor mass fraction. Under these assumptions, we have derived a new analytical solution for the vapor mass fraction field in the gas phase and the temperature field in the gas and liquid

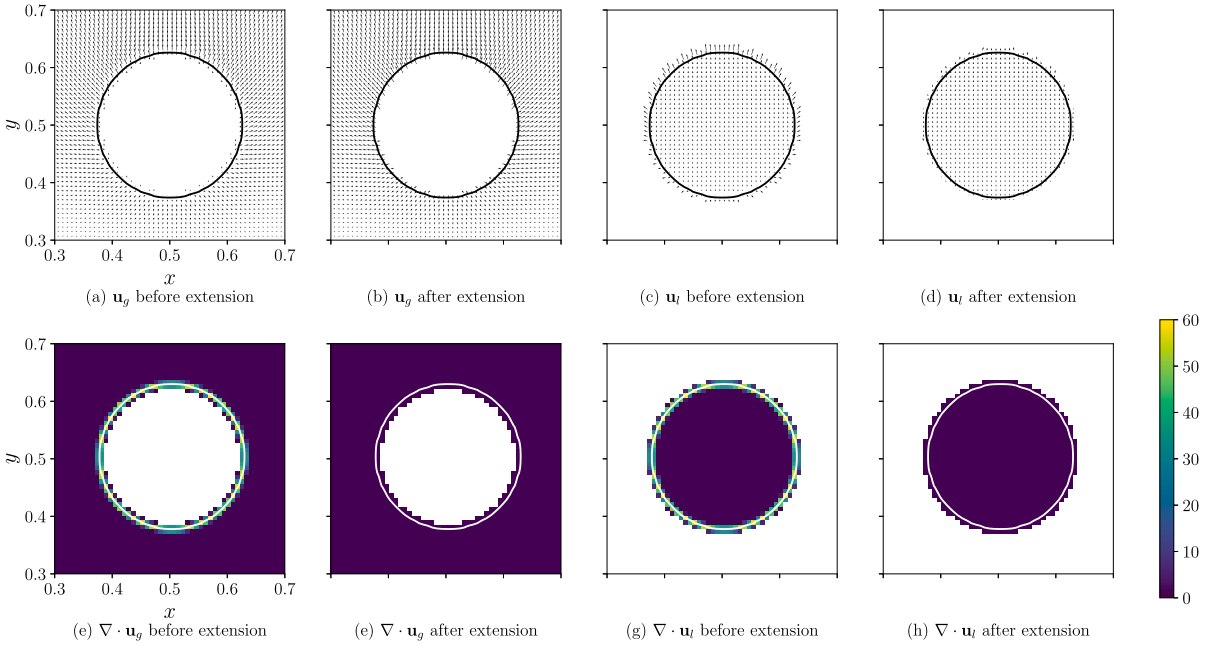

Fig. 15. Detail of the liquid- and gas-velocity vectors and their respective divergence around the evaporating droplet with $\rho_l/\rho_g = 10$ at $t = 0$. The quantities are shown before and after the divergence-free velocity extension procedure described in Section 3.3.

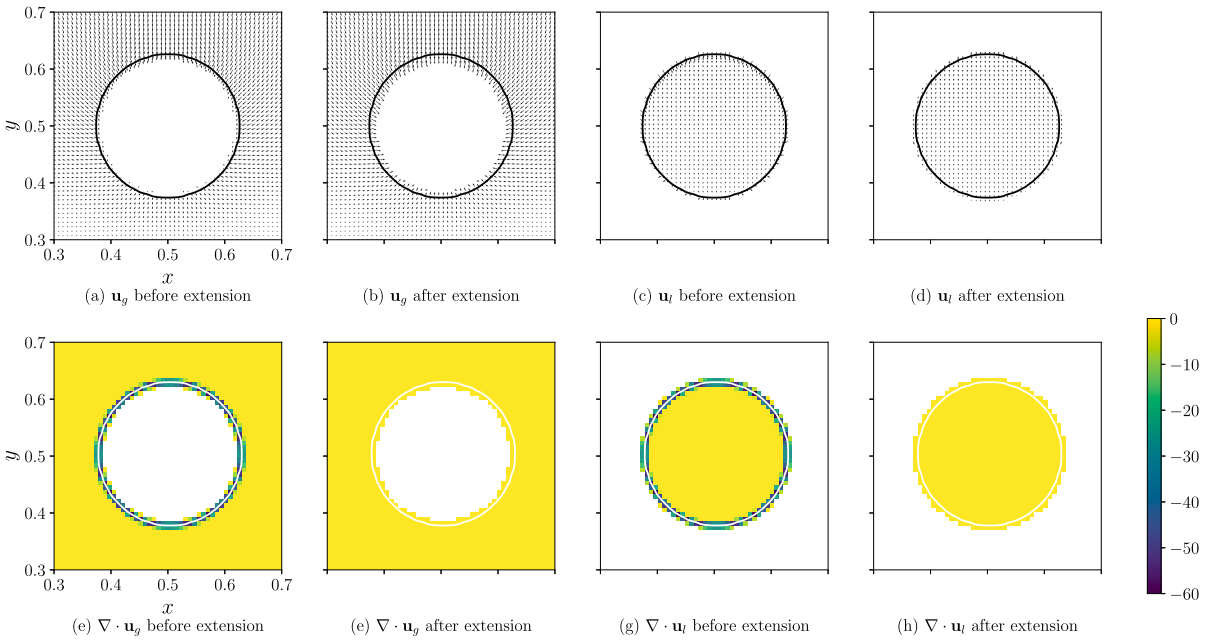

Fig. 16. Detail of the liquid- and gas-velocity vectors and their respective divergence around the condensing droplet with $\rho_l/\rho_g = 10$ at $t = 0$. The quantities are shown before and after the divergence-free velocity extension procedure described in Section 3.3.

Table 3
Error in the vaporization rate per unit area $E_{\dot{m}''}$ as a function of the grid spacing Δx for 1D Stefan problem.

Δx	$E_{\dot{m}''}$	Rate
1/16	3.30e-3	–
1/32	7.49e-4	2.20
1/64	1.73e-4	2.17

phases. The derivation for the analytical solution of the temperature field is presented in Appendix A. The solution for the vapor mass fraction field is

$$Y_v(x) = 1 - (1 - Y_{v,sat})\left(\frac{1 - Y_{v,L}}{1 - Y_{v,sat}}\right)^{(2x-1)/L}, \tag{55}$$

where L is the length of the gas-liquid domain and the gas-liquid interface is located at $x = L/2$.

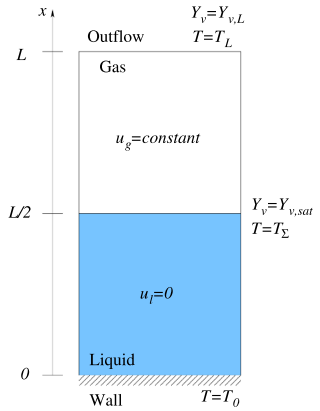

Fig. 17. Domain for 1D Stefan flow.

The solution for the temperature at the interface ($x = L/2$) is (Eq. (A.31))

$$T_\Sigma = \frac{T_L + \frac{1}{\mathrm{Ste}}\left(1 - e^{K(3L/2)}\right) + \frac{2\,\mathrm{Le}\,T_0}{\dot{m}'' L}\frac{k_l}{k_g}\left(e^{K(3L/2)} - 1\right)}{1 + \frac{2\,\mathrm{Le}}{\dot{m}'' L}\frac{k_l}{k_g}\left(e^{K(3L/2)} - 1\right)}, \tag{56}$$

where K is a function given by

$$K(x) = \frac{\dot{m}''(x - L)}{\mathrm{Le}}, \tag{57}$$

and where Le is the Lewis number,

$$\mathrm{Le} = \frac{\tilde{k}_{\mathrm{ref}}}{\tilde{\rho}_{\mathrm{ref}}\tilde{D}_{gv}\tilde{c}_{p,\mathrm{ref}}} = \frac{\mathrm{Sc}}{\mathrm{Pr}}. \tag{58}$$

The solution to the temperature field in the liquid phase ($0 < x \leq L/2$) is (Eq. (A.18))

$$T(x) = \frac{2(T_\Sigma - T_0)}{L}x + T_0 \tag{59}$$

and in the gas phase ($L/2 < x < L$) the solution is (Eq. (A.18))

$$T(x) = T_L e^{K(x)} + T_\Sigma\left(1 - e^{K(x)}\right) + \frac{1}{\mathrm{Ste}}\left(e^{K(x)} - 1\right) + \frac{2\,\mathrm{Le}}{\dot{m}'' L}\frac{k_l}{k_g}\left[T_0\left(1 - e^{K(x)}\right) + T_\Sigma\left(e^{K(x)} - 1\right)\right]. \tag{60}$$

The conditions for the test are $L = 1$, $\mathrm{Re} = 200$, $\mathrm{Sc} = 1$, $\mathrm{Pr} = 0.5$, $\mathrm{Ste} = 0.5$, $Y_{v,L} = 0$, $Y_{v,sat} = 0.5$, $T_0 = 0.7$, $T_L = 0.8$, $\rho_l/\rho_g = 10^{10}$, $\mu_l/\mu_g = 4$, $c_{p,l}/c_{p,g} = 10^{-9}$, and $k_l/k_g = 4$. Note that ρ_l/ρ_g is made sufficiently large such that the interface is practically stationary and $c_{p,l}/c_{p,g}$ is made sufficiently small such that the heat capacities of the liquid and gas phase are of the same order of magnitude. To test the convergence properties of the schemes, we performed this test case on three grids $N = 16$, 32, and 64.

Fig. 18 shows the profiles of the vapor mass fraction and temperature compared to the analytical solution on the finest grid ($N = 64$). The results show that both $Y_v(x)$ and $T(x)$ are in excellent agreement with the analytical solution. Fig. 18(a) shows that the exponential $Y_v(x)$ profile (Eq. (55)) is captured for the 1D Stefan flow. Fig. 18(b) shows that the temperature profile $T(x)$ is correctly computed in both the liquid ($x < L/2$) and gas ($x \geq L/2$) phases. At the interface, the scheme accurately captures the jump in $\partial T/\partial x$ due to $k_l/k_g \neq 0$. Furthermore, the correct interface temperature T_Σ is predicted, which indicates that the singular source/sink term (last term in Eq. (5)) is captured accurately by the discretization presented in Eq. (50).

Table 4 shows the L_1 error of the vapor mass fraction (E_{Y_v}) and temperature (E_T) profiles as function of the grid spacing Δx. The table shows that the computation of the the vapor mass fraction $Y_v(x)$ is between first- and second-order accurate. The computation of the temperature $T(x)$ is first-order accurate.

4.4. Spatial convergence: 2D evaporating capillary wave

In this section, we report the results of the spatial convergence rate of the numerical solution for the case when $\dot{m}''$ is fixed to a constant value and when $\dot{m}'' = \dot{m}''(Y_v)$. In the former case, the continuity Eq. (1) and momentum Eq. (3) are coupled, but the energy Eq. (5) is decoupled, whereas, in the latter case, all three equations are fully coupled, Y_v evolves according to Eq. (6), and $\dot{m}''$ is computed dynamically via Eq. (2). We chose the 2D capillary wave test case, which has a well-known analytical solution in the

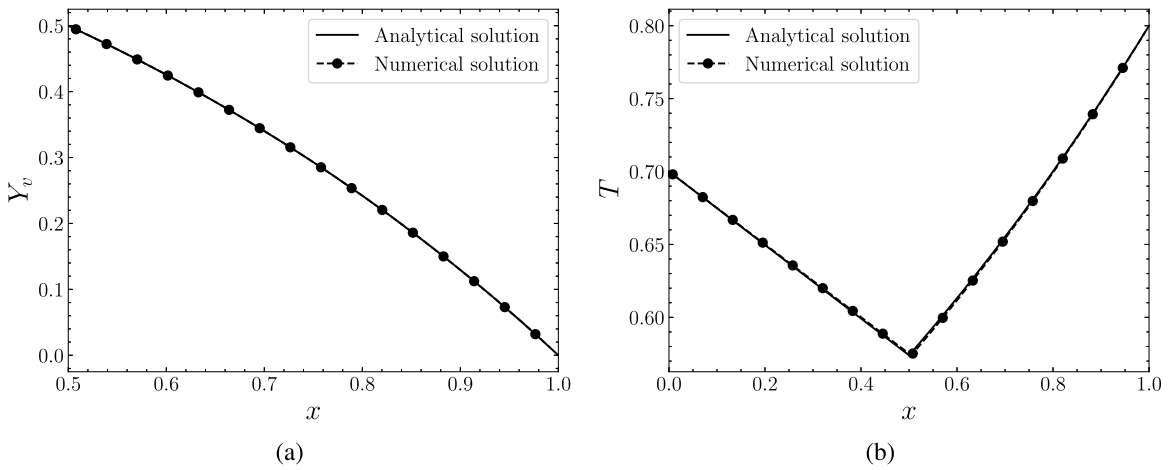

Fig. 18. Comparison of the numerical and analytical solutions of (a) the vapor mass fraction and (b) the temperature for 1D Stefan flow depicted in Fig. 17. The numerical results were obtained for $N = 64$ and are plotted against the analytical solutions, Eqs. (55), (59) and (60).

Table 4
L_1 error norm of the vapor mass fraction and temperature as a function of the grid spacing Δx for the 1D Stefan flow depicted in Fig. 17.

Δx	E_{Y_v}	Rate	E_T	Rate
1/16	2.22e-5	–	1.83e-3	–
1/32	5.30e-6	2.09	9.52e-4	0.97
1/64	1.27e-6	2.09	4.81e-4	0.99

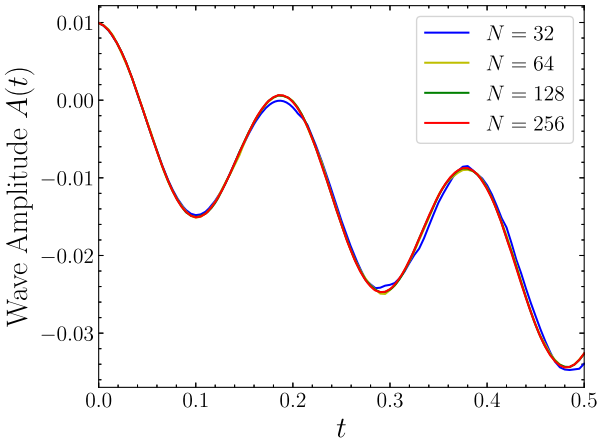

Fig. 19. Time development of the capillary wave amplitude for different mesh resolutions and $\dot{m}''$ constant.

absence of phase change [41]. Instead of pursuing an analytical solution of the vaporizing capillary wave, we have computed the convergence rate by computing the difference between successive solutions.

The problem setup consists of two immsicible fluids separated by an interface that is initialized with a sinusoid with wavelength λ and initial wave amplitude A_0. The computational domain is $x \in [0, 1]$ and $y \in [0, 1]$ and a uniform mesh is used with equal number of grid points in x and y. Periodic boundary conditions are applied in the x direction, a wall boundary condition is used at $y = 0$ and an outflow boundary condition at $y = 1$. The first case we consider is for $\dot{m}''$ constant. The physical parameters are Re = 50, We = 0.02, Sc = 1, $\rho_l/\rho_g = 10$, $\mu_l/\mu_g = 1$, $\dot{m}'' = 25$, and $A_0 = 0.01$. We performed four test-cases in the which the number of grid points in each direction is $N = 32$, 64, 128, and 256, respectively. The time step is limited by the period of the shortest numerical capillary wave and is set as $\Delta t/\Delta x = 0.005$, where $\Delta x = 1/N$.

Fig. 19 shows the amplitude of the capillary wave for increasing number of grid points. The results show that the capillary wave oscillates and recedes simultaneously due to phase change. The figure also shows that the numerical solution converges. To quantify the convergence rate, we compute the L_1 norm of the difference between successive solutions of u, v, and A. The L_2 norms and associated convergence rates are reported in Table 5. The table shows that the convergence rates range between 1.19 and 1.95, thus the computation of u, v, and A has an accuracy between first and second order.

The second test case we consider is when $\dot{m}''$ is computed dynamically from the local vapor mass fraction field, $\dot{m}'' = \dot{m}''(Y_v)$ as described in Section 3.4 using Eq. (32). The physical parameters are Re = 25, We = 0.02, Sc = 1, Pr = 1, Ste = 10, $\text{Ste}_c = 7.43 \times 10^{-2}$, $T_{\text{boil}} = 1.3$, $\rho_l/\rho_g = 10$, $\mu_l/\mu_g = 1$, $c_{p,l}/c_{p,g} = 1$, $k_l/k_g = 4$, and $M_v/M_a = 1$, and $A_0 = 0.01$. The meshes and time step used for this second test case are identical to those adopted for the first test case in which $\dot{m}''$ was kept constant.

Fig. 20 shows the amplitude of the capillary wave for increasing N. The results are very similar to the first case in this section when $\dot{m}''$ was constant. Table 6 shows the L_2 norm of the difference between successive solutions and convergence rates for u, v, Y_v, and T. The table shows that the convergence rates range from 0.99 to 2.11, thus, showing that all quantities (u, v, Y_v, and T) are computed with an accuracy that is between first and second order.

Table 5
L_2 norm of the difference between successive solutions of u and v components of velocity (E_u and E_v) and the amplitude A of the capillary wave (E_A) as a function of the grid spacing Δx for $\dot{m}''$ constant at time $t = 0.5$. For example, the second row represents the L_1 norm of the difference between the $N = 64$ and $N = 128$ solution.

Δx	E_u	Rate	E_v	Rate	E_A	Rate
1/64	9.43e-5	–	4.60e-4	–	9.44e-5	–
1/128	2.69e-5	1.75	1.61e-4	1.43	2.13e-5	2.22
1/256	9.88e-6	1.36	6.01e-5	1.34	5.56e-6	1.91

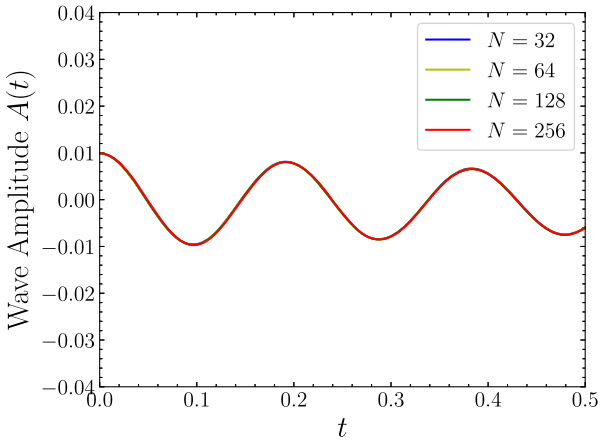

Fig. 20. Time development of the capillary wave amplitude for different mesh resolutions and $\dot{m}'' = \dot{m}''(Y_v)$.

Table 6
L_2 norm of the difference between successive solutions of the u and v components of velocity (E_u and E_v), the capillary wave amplitude A (E_A), the vapor mass fraction Y_v (E_{Y_v}), and temperature T (E_T) as a function of the grid spacing Δx for $\dot{m}'' = \dot{m}''(Y_v)$ computed using Eq. (32) at time $t = 0.5$.

Δx	E_u	Rate	E_v	Rate	E_{Y_v}	Rate	E_T	Rate
1/64	9.18e-5	–	1.51e-3	–	3.98e-5	–	7.81e-7	–
1/128	3.82e-5	1.20	5.64e-4	1.34	1.42e-5	1.41	3.69e-7	1.06
1/256	1.81e-5	1.05	3.33e-4	0.85	5.15e-6	1.37	9.90e-8	1.87

4.5. *Verification of fully coupled solver: 3D evaporating droplet at rest*

In this section, we verify the fully-coupled solver (as illustrated in Fig. 3) by solving the governing Eq. (1), (3), (5), and (6) with the method described in Section 3 for an isolated liquid fuel droplet undergoing evaporation. We compare the numerical results to the D^2 law [42,43].

We consider a spherical decane droplet in a cubic domain. Periodic boundary conditions are applied in the two horizontal directions and outflow boundary conditions are applied in the vertical direction. Initially, the gas and liquid velocities are zero, the temperature field is uniform, and the gas phase is devoid of vapor. In our simulation, the domain has length $\tilde{L} = 320$ μm on all sides, the initial droplet diameter is $\tilde{D}_0 = 20$ μm, and 256^3 grid points. The parameters and initial conditions are Re = 200, Sc = 0.33, Pr = 0.69, Ste = 1.19, $\text{Ste}_c = 6.82 \times 10^{-2}$, $\tilde{T}_{\text{boil}} = 557.15$ K, $\tilde{T}_l = \tilde{T}_g = 400$ K, $\rho_l/\rho_g = 79.19$, $\mu_l/\mu_g = 18.4$, $c_{p,l}/c_{p,g} = 2.42$, $k_l/k_g = 4.316$, and $M_v/M_a = 4.91$. For this fully-coupled 3D simulation, we set a tolerance of 10^{-7} for the linear solver in the velocity extension routines (Section 3.3). This larger tolerance was chosen to obtain a speedup of the numerical solution. Since the tolerance was set to 10^{-7}, then, the mass conservation error is approximately 10^{-7}, as the accuracy of the VoF method depends on the accuracy of the discrete divergence-free condition of the extended liquid velocity field. This choice maintains numerical stability and the prescribed accuracy, as discussed in Section 3.3.

To verify the accuracy of the simulation we compute the mean Sherwood number of the droplet as a function of time, and compare it to the exact, steady-state solution for a static 3D sphere. The droplet Sherwood number is calculated as

$$\text{Sh}(t) = \text{Re}\ \text{Sc}\ D(t)\ h_{\text{mass}}(t), \tag{61}$$

where $D(t)$ is the droplet diameter, and $h_{\text{mass}}(t)$ is the average mass transfer coefficient calculated as

$$h_{\text{mass}}(t) = \frac{\dot{M}(t)}{S(t)\ \rho_g (Y_{v,sat} - Y_{v,\infty})}, \tag{62}$$

where $\dot{M}(t)$ is the instantaneous rate of change of droplet mass, $S(t)$ is the droplet surface area, and $Y_{v,\infty}$ is the vapor mass fraction in the far field (a constant).

Fig. 21 shows the time evolution of the Sherwood number (Sh) and the normalized droplet diameter squared $(D/D_0)^2$. Fig. 21(a) shows that the Sherwood number is slightly higher than the correct asymptotic solution of Sh = 2. Fig. 21(b) shows that after an initial transient period, $(D/D_0)^2$ decays linearly in time, which verifies that our simulation follows the D^2-law for the isolated static droplet.

5. Summary and Conclusions

We have developed FastP*PC, a coupled volume-of-fluid and pressure-correction flow solver for incompressible gas-liquid flows with phase change which is an extension of FastP* [26]. The method specifically addresses flows in which the liquid is monocomponent

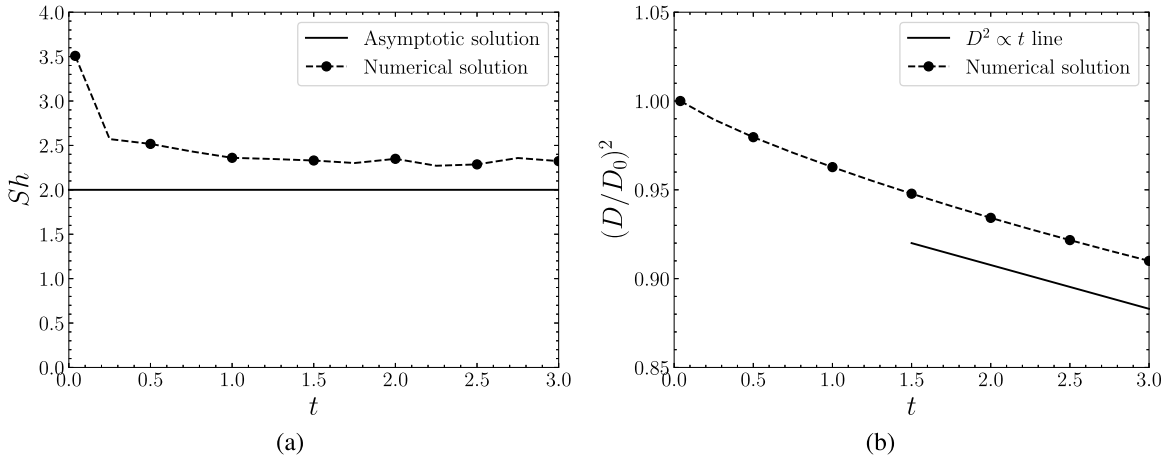

Fig. 21. Comparison of the numerical and analytical solutions for the time evolution of (a) the Sherwood number (b) the normalized droplet diameter squared of a vaporizing 3D fuel droplet.

and the gas phase is bicomponent, e.g. a decane droplet evaporating in oxygen. A summary of the main contributions of this work follows.

1. A novel method for capturing the gas-liquid interface in the presence of heat and mass transfer within the VoF framework is presented (Section 3.2). The main advantage of the approach, compared to existing VoF methods for phase change, is that it does not require a projection step of the liquid velocity to divergence-free space nor does it require any ad hoc smoothing or redistribution of volume sources/sinks. To achieve this, the key step was developing a novel divergence-free extrapolation technique of the velocity field (Section 3.3).
2. The VoF method achieves mass conservation in the presence of evaporation and condensation, with accuracy determined by the choice of tolerance for the divergence-free liquid velocity extension. Practical solver tolerances of 10^{-7} to 10^{-10} yield minor mass conservation errors while maintaining numerical stability, as shown in Sections 4 and 4.5. Outside the interfacial region, mass is conserved to machine precision by using an FFT-based, fast Poisson solver in both phases.
3. A new discretization of the vapor mass conservation equation in the vicinity of the gas-liquid interface is developed (Section 3.5). This technique makes it possible to apply a Dirichlet boundary condition with high order of accuracy at the interface.
4. By computing and using the VoF function at staggered grid locations, the flow solver maintains a sharp representation of the gas-liquid interface, and yields jumps in velocity and temperature gradient that occur over a distance on the order of one grid cell (Section 4.3).
5. A new analytical solution for the 1D Stefan flow problem was derived for a fluid system consisting of a monocomponent-liquid and a bicomponent-gas phase Section 4.3. Solutions for the vapor mass fraction Eq. (55), gas temperature Eq. (59), and liquid temperature Eq. (60) profiles were shown. This test case will be useful for verifying future two-phase flow solvers that model phase change.

We have demonstrated that the VoF advection method can be used to simulate evaporating and condensing droplets. Using a normal probe approach that uses second-order Lagrange interpolating polynomials, we have computed the mass flux to second-order accuracy. The new approach for applying the Dirichlet boundary condition at the interface was shown to be between first- and second-order accurate for computing the vapor mass fraction field. We also tested a 3D evaporating droplet at rest and showed that the Sherwood number approached the correct asymptotic value and that the droplet diameter followed the D^2-law. We should note that FastP* [26] has been successfully tested for density ratios of the order of 10^4, and that the solution of FastP*PC agrees to machine precision with the analytical solution for the 1D evaporation of the liquid pool for density ratios up to 10^4, but, for 2D and 3D cases, FastP*PC has been tested to be stable up to density ratios of 500 with mass conserved within $\mathcal{O}(10^{-7}, 10^{-10})$.

CRediT authorship contribution statement

Michael S. Dodd: Writing – review & editing, Writing – original draft, Software, Methodology, Investigation, Conceptualization; **Pablo Trefftz-Posada:** Writing – review & editing, Visualization, Validation, Software, Methodology, Investigation, Formal analysis, Data curation; **Antonino Ferrante:** Writing – review & editing, Writing – original draft, Methodology, Investigation, Supervision, Resources, Project administration, Funding acquisition, Conceptualization.

Data availability

Data will be made available on request.

Declaration of competing interest

The authors declare that they have no known competing financial interests or personal relationships that could have appeared to influence the work reported in this paper.

Acknowledgments

This work was partially supported by the National Science Foundation (NSF) CAREER Award, grant no. ACI-1054591. M.S.D. was also partially supported by the Clairmont Egtvedt Fellowship and the Louis and Katherine Marsh Fellowship from the College of Engineering at the University of Washington (UW), Seattle. The numerical simulations were performed in part on Hyak, high-performance computer cluster at UW, and in part on the Extreme Science and Engineering Discovery Environment (XSEDE, Towns et al. 2014) under XRAC grant no. TG-CTS100024. XSEDE is supported by National Science Foundation grant no. ACI-1053575. We specifically acknowledge the Texas Advanced Computing Center (TACC) at The University of Texas at Austin (http://www.tacc.utexas.edu) and the University of Tennessee and Oak Ridge National Laboratory's Joint Institute for Computational Sciences (http://www.jics.utk.edu) for providing HPC resources that have contributed to the research results reported within this paper. The authors specifically acknowledge the assistance of the XSEDE Extended Collaborative Support Service [43] team members, J. Alameda and D. Adams, of the National Center for Supercomputing Applications (NCSA) at the University of Illinois at Urbana-Champaign. The authors also acknowledge Mr. Nithin Adidela for proofreading the article.

Appendix A. Analytical solution to the 1D non-dimensional internal energy equation during steady-state Stefan flow

In this section we derive the analytical solution to the 1D non-dimensional internal energy equation during steady-state Stefan flow. We consider the 1D Stefan flow problem illustrated in Fig. A.1, where the gas phase is denoted by $m = g$ and the liquid phase is denoted by $m = l$. Dirichlet conditions for vapor mass fraction and temperature are applied at the outflow boundary. At the lower wall, a Dirichlet boundary conditions is applied for temperature. At the interface, a Dirichlet boundary condition is applied for the saturated vapor mass fraction. We begin with the 1D non-dimensional internal energy equation,

$$\frac{\partial T_m}{\partial t} + u\frac{\partial T_m}{\partial x} = \frac{1}{\mathrm{RePr}}\frac{k_m}{\rho_m c_{p,m}}\frac{\partial^2 T_m}{\partial x^2}, \quad \text{for } m = g \text{ or } l. \tag{A.1}$$

At steady state $T_m = T_m(x)$, so Eq. (A.1) is rewritten as

$$u_m\frac{\mathrm{d}T_m}{\mathrm{d}x} = \frac{1}{\mathrm{RePr}}\frac{k_m}{\rho_m c_{p,m}}\frac{\partial^2 T_m}{\partial x^2}, \quad \text{for } m = g \text{ or } l. \tag{A.2}$$

Next, we derive the non-dimensional jump conditions for the heat flux across the interface which will serve as a boundary condition at the interface. The jump condition for heat flux in dimensional form is

$$\tilde{\dot{m}}''\tilde{h}_{lg} = \tilde{k}_l\frac{\partial\tilde{T}_l}{\partial\hat{n}} - \tilde{k}_g\frac{\partial\tilde{T}_g}{\partial\hat{n}}. \tag{A.3}$$

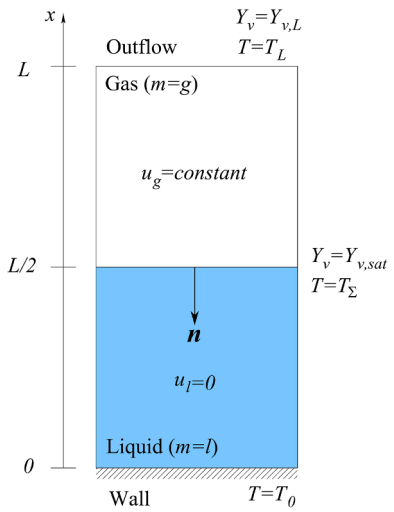

Fig. A.1. Domain for 1D Stefan flow.

For the flow problem shown in Fig. A.1, $\frac{\partial}{\partial \hat{n}} = -\frac{\mathrm{d}}{\mathrm{d}x}$, so we rewrite Eq. (A.3) as

$$\tilde{\dot{m}}'' \tilde{h}_{lg} = \tilde{k}_g \frac{\mathrm{d}\tilde{T}_g}{\mathrm{d}\tilde{x}} - \tilde{k}_l \frac{\mathrm{d}\tilde{T}_l}{\mathrm{d}\tilde{x}}. \tag{A.4}$$

We introduce the following non-dimensional variables:

$$\dot{m}'' = \frac{\tilde{\dot{m}}'' \tilde{L}_{\mathrm{ref}}}{\tilde{D}_{gv}\tilde{\rho}_{\mathrm{ref}}}, \quad k = \frac{\tilde{k}}{\tilde{k}_{\mathrm{ref}}}, \quad T = \frac{\tilde{T}}{\tilde{T}_{\mathrm{ref}}}, \quad \frac{\mathrm{d}}{\mathrm{d}x} = \tilde{L}_{\mathrm{ref}} \frac{\mathrm{d}}{\mathrm{d}\tilde{x}}. \tag{A.5}$$

Introducing Eq. (A.5) into Eq. (A.4) yields

$$\frac{\tilde{h}_{lg}\tilde{D}_{gv}}{\tilde{L}_{\mathrm{ref}}\tilde{U}_{\mathrm{ref}}\tilde{c}_{p,\mathrm{ref}}\tilde{T}_{\mathrm{ref}}} \dot{m}'' = \frac{\tilde{k}_{\mathrm{ref}}}{\tilde{L}_{\mathrm{ref}}\tilde{\rho}_{\mathrm{ref}}\tilde{U}_{\mathrm{ref}}\tilde{c}p,\,\mathrm{ref}} \left(k_g \frac{\mathrm{d}T_g}{\mathrm{d}x} - k_l \frac{\mathrm{d}T_l}{\mathrm{d}x} \right), \tag{A.6}$$

and, substituting the non-dimensional quantites from Eqs. (7) and (58) into Eq. (A.6) results in the non-dimensional jump conditions for the heat flux:

$$\frac{1}{\mathrm{Ste}} \dot{m}'' = \mathrm{Le} \left(k_g \frac{\mathrm{d}T_g}{\mathrm{d}x} - k_l \frac{\mathrm{d}T_l}{\mathrm{d}x} \right). \tag{A.7}$$

The governing equations for the gas and liquid phases are

$$\text{Gas:} \quad u_g \frac{\mathrm{d}T_g}{\mathrm{d}x} = \frac{1}{\mathrm{Re\,Pr}} \frac{k_g}{\rho_g c_{p,g}} \frac{\mathrm{d}^2 T_g}{\mathrm{d}x^2}, \tag{A.8}$$

$$\text{Liquid:} \quad 0 = \frac{1}{\mathrm{Re\,Pr}} \frac{k_l}{\rho_l c_{p,l}} \frac{\mathrm{d}^2 T_l}{\mathrm{d}x^2}, \tag{A.9}$$

where the left-hand side of Eq. (A.9) is 0 because $u_l = 0$. The boundary conditions for the flow problem are

$$\text{At } x = 0; \quad T_l = T_0, \tag{A.10}$$

$$\text{At } x = L; \quad T_g = T_0, \tag{A.11}$$

$$\text{At } x = L/2; \quad T_g = T_l = T_\Sigma, \tag{A.12}$$

$$\text{At } x = L/2; \quad \frac{1}{\mathrm{Ste}} \dot{m}'' = \mathrm{Le} \left(k_g \frac{\mathrm{d}T_g}{\mathrm{d}x} - k_l \frac{\mathrm{d}T_l}{\mathrm{d}x} \right), \tag{A.13}$$

The solution begins by integrating Eq. (A.9) once with respect to x:

$$c_1 = \frac{1}{\mathrm{Re\,Pr}} k_l \frac{\mathrm{d}T_l}{\mathrm{d}x}. \tag{A.14}$$

Eq. (A.14) shows that $\frac{\mathrm{d}T_l}{\mathrm{d}x}$ is constant for $0 < x < L/2$. We integrate Eq. (A.14) again with respect to x and flip the left and right-hand sides to yield

$$\frac{1}{\mathrm{Re\,Pr}} k_l T_l(x) = c_1 x + c_2. \tag{A.15}$$

Using Eq. (A.14) and Eq. (A.10) and multiplying through by $\frac{\mathrm{Re\,Pr}}{k_l}$, Eq. (A.15) can be rewritten as

$$T_l(x) = \frac{\mathrm{d}T_l}{\mathrm{d}x} x + T_0. \tag{A.16}$$

Because $\frac{\mathrm{d}T_l}{\mathrm{d}x}$ is constant, applying the boundary conditions in Eqs. (A.10) and (A.12) gives

$$\frac{\mathrm{d}T_l}{\mathrm{d}x} = \frac{2\left(T_\Sigma - T_0\right)}{L}, \tag{A.17}$$

which when substituted into Eq. (A.16) yields

$$T_l(x) = \frac{2\left(T_\Sigma - T_0\right)}{L} x + T_0, \quad \text{for } 0 < x < L/2, \tag{A.18}$$

which is the result reported in Eq. (59) in Section 4.3.

Next, we consider the gas phase. We begin by noting that

$$\tilde{\rho}_g \tilde{u}_g = \tilde{\dot{m}}''. \tag{A.19}$$

By substituting non-dimensional values and quantities from Eqs. (7) and (A.5) and dividing through by ρ_g, Eq. (A.19) can be rewritten as

$$u_g = \frac{1}{\mathrm{Re\,Sc}} \frac{\dot{m}''}{\rho_g}. \tag{A.20}$$

Substituting Eq. (A.20) into (A.8), rearranging terms, and multiplying through by (Re Sc) we obtain

$$c_{p,g}\dot{m}''\frac{\mathrm{d}T_g}{\mathrm{d}x} = \mathrm{Le}\ k_g\frac{\mathrm{d}^2T_g}{\mathrm{d}x^2}, \tag{A.21}$$

where Le is the Lewis number (Eq. (58)), i.e., Le = Sc/Pr. We integrate Eq. (A.21) with respect to x to obtain

$$c_{p,g}\dot{m}''T_g(x) = \mathrm{Le}\ k_g\frac{\mathrm{d}T_g}{\mathrm{d}x} + c_3. \tag{A.22}$$

Evaluating Eq. (A.22) at $x = L/2$ and applying boundary conditions (A.12) and (A.13) yields

$$c_{p,g}\dot{m}''T_\Sigma = \frac{1}{\mathrm{Ste}}\dot{m}'' + \mathrm{Le}\ k_l\frac{\mathrm{d}T_l}{\mathrm{d}x}\Big|_\Sigma + c_3. \tag{A.23}$$

Solving for c_3 in Eq. (A.23), substituting into Eq. (A.21), and using Eq. (A.17) we obtain

$$c_{p,g}\dot{m}''T_g(x) = \mathrm{Le}\ k_g\frac{\mathrm{d}T_g}{\mathrm{d}x} + \dot{m}''\left(c_{p,g}T_\Sigma - \frac{1}{\mathrm{Ste}}\right) - \mathrm{Le}\ k_l\frac{2\left(T_\Sigma - T_0\right)}{L}. \tag{A.24}$$

We perform separation of variables to the derivative term of Eq. (A.24) and rearrange terms to yield

$$\frac{\mathrm{d}T_g}{T_g(x) + \frac{1}{c_{p,g}}\left(\frac{1}{\mathrm{Ste}} - c_{p,g}T_\Sigma\right) + \frac{\mathrm{Le}\ k_l}{c_{p,g}\dot{m}''}\left(\frac{2(T_\Sigma - T_0)}{L}\right)} = \frac{c_{p,g}\dot{m}''}{\mathrm{Le}\ k_g}\mathrm{d}x. \tag{A.25}$$

We integrate both sides of Eq. (A.25) to obtain

$$\ln\left\{T_g(x) + \frac{1}{c_{p,g}}\left(\frac{1}{\mathrm{Ste}} - c_{p,g}T_\Sigma\right) + \frac{\mathrm{Le}\ k_l}{c_{p,g}\dot{m}''}\left(\frac{2(T_\Sigma - T_0)}{L}\right)\right\} = \frac{c_{p,g}\dot{m}''}{\mathrm{Le}\ k_g}x + c_4 \tag{A.26}$$

Evaluating Eq. (A.26) at $x = L$ and applying boundary condition (A.11) yields

$$\ln\left\{T_L + \frac{1}{c_{p,g}}\left(\frac{1}{\mathrm{Ste}} - c_{p,g}T_\Sigma\right) + \frac{\mathrm{Le}\ k_l}{c_{p,g}\dot{m}''}\left(\frac{2(T_\Sigma - T_0)}{L}\right)\right\} = \frac{c_{p,g}\dot{m}''}{\mathrm{Le}\ k_g}L + c_4. \tag{A.27}$$

Solving for c_4 in Eq. (A.27), substituting into Eq. (A.26) and combining like terms we obtain

$$\begin{aligned}&\ln\left\{T_g(x) + \frac{1}{c_{p,g}}\left(\frac{1}{\mathrm{Ste}} - c_{p,g}T_\Sigma\right) + \frac{\mathrm{Le}\ k_l}{c_{p,g}\dot{m}''}\left(\frac{2(T_\Sigma - T_0)}{L}\right)\right\}\\ &\quad= \frac{c_{p,g}\dot{m}''}{\mathrm{Le}\ k_g}(x - L) + \ln\left\{T_L + \frac{1}{c_{p,g}}\left(\frac{1}{\mathrm{Ste}} - c_{p,g}T_\Sigma\right) + \frac{\mathrm{Le}\ k_l}{c_{p,g}\dot{m}''}\left(\frac{2(T_\Sigma - T_0)}{L}\right)\right\}.\end{aligned} \tag{A.28}$$

Exponentiating both sides of Eq. (A.28) and rearranging terms yields

$$\begin{aligned}T_g(x) =& T_L e^{K(x)} + T_\Sigma\left(1 - e^{K(x)}\right) + \frac{1}{c_{p,g}\ \mathrm{Ste}}\left(e^{K(x)} - 1\right)\\ &+ \frac{2\ \mathrm{Le}\ k_l}{c_{p,g}\dot{m}''L}\left[T_\Sigma\left(e^{K(x)} - 1\right) + T_0\left(1 - e^{K(x)}\right)\right], \quad \text{for } L/2 < x < L,\end{aligned} \tag{A.29}$$

where $K(x) = \dfrac{c_{p,g}\dot{m}''}{\mathrm{Le}\ k_g}(x - L)$. Assigning the gas phase quantities a unity value, $k_g = c_{p,g} = 1$, we obtain

$$\begin{aligned}T_g(x) =& T_L e^{K(x)} + T_\Sigma\left(1 - e^{K(x)}\right) + \frac{1}{\mathrm{Ste}}\left(e^{K(x)} - 1\right)\\ &+ \frac{2\ \mathrm{Le}}{\dot{m}''L}\frac{k_l}{k_g}\left[T_0\left(1 - e^{K(x)}\right) + T_\Sigma\left(e^{K(x)} - 1\right)\right], \quad \text{for } L/2 < x < L,\end{aligned} \tag{A.30}$$

which is the result reported in Eq. (60) in Section 4.3. Lastly, to solve for T_Σ, we evaluate Eq. (A.30) at $x = L/2$ and use a symbolic solver to yield

$$T_\Sigma = \frac{T_L + \frac{1}{\mathrm{Ste}}\left(1 - e^{K(3L/2)}\right) + \frac{2\ \mathrm{Le}\ T_0}{\dot{m}''L}\frac{k_l}{k_g}\left(e^{K(3L/2)} - 1\right)}{1 + \frac{2\ \mathrm{Le}}{\dot{m}''L}\frac{k_l}{k_g}\left(e^{K(3L/2)} - 1\right)}, \tag{A.31}$$

which is the result reported in Eq. (56) in Section 4.3.

References

[1] S. Mirjalili, S.S. Jain, M.S. Dodd, Interface-capturing methods for two-phase flows: An overview and recent developments, Center for Turbul. Res. Ann. Res. Briefs (2017) 117–135.
[2] M. Irfan, M. Muradoglu, A front tracking method for direct numerical simulation of evaporation process in a multiphase system, J. Comput. Phys. 337 (2017) 132–153.
[3] G. Son, V.K. Dhir, Numerical simulation of film boiling near critical pressures with a level set method, J. Heat Transf. 120 (1) (1998) 183–192.
[4] F. Gibou, L. Chen, D. Nguyen, S. Banerjee, A level set based sharp interface method for the multiphase incompressible Navier–Stokes equations with phase change, J. Comput. Phys. 222 (2) (2007) 536–555.
[5] L. Rueda Villegas, R. Alis, M. Lepilliez, S. Tanguy, A ghost fluid/level set method for boiling flows and liquid evaporation: application to the Leidenfrost effect, J. Comput. Phys. 316 (2016) 789–813.
[6] S. Tanguy, T. Ménard, A. Berlemont, A Level Set Method for vaporizing two-phase flows, J. Comput. Phys. 221 (2) (2007) 837–853.
[7] L.C. Malan, R. Scardovelli, S. Zaleski, Using extrapolation techniques in VOF methodology to model expanding bubbles, Procedia IUTAM 15 (2015) 228–235.
[8] T. Long, J. Pan, S. Zaleski, An edge-based interface tracking (EBIT) method for multiphase flows with phase change, J. Comput. Phys. 513 (2024) 113159.
[9] S.W.J. Welch, J. Wilson, A volume of fluid based method for fluid flows with phase change, J. Comput. Phys. 160 (2) (2000) 662–682.
[10] J. Schlottke, B. Weigand, Direct numerical simulation of evaporating droplets, J. Comput. Phys. 227 (10) (2008) 5215–5237.
[11] S. Hardt, F. Wondra, Evaporation model for interfacial flows based on a continuum-field representation of the source terms, J. Comput. Phys. 227 (11) (2008) 5871–5895.
[12] D.L. Youngs, Time-dependent multi-material flow with large fluid distortion, Numer. Methods Fluid Dyn. 1 (1) (1982) 41–51.
[13] M.S. Lee, A. Riaz, V. Aute, Direct numerical simulation of incompressible multiphase flow with phase change, J. Comput. Phys. 344 (2017) 381–418.
[14] A. Ferrante, M.S. Dodd, Towards a mass-conserving volume-of-fluid method for incompressible gas-liquid flows with phase change, Bull. Amer. Phys. Soc. 63 (2018).
[15] B. Duret, R. Canu, J. Reveillon, F.X. Demoulin, A pressure based method for vaporizing compressible two-phase flows with interface capturing approach, Int. J. Multiphase Flow 108 (2018) 42–50.
[16] Y. Wang, V. Yang, Vaporization of liquid droplet with large deformation and high mass transfer rate, I: constant-density, constant-property case, J. Comput. Phys. 392 (2019) 56–70.
[17] Y. Wang, X. Chen, X. Wang, V. Yang, Vaporization of liquid droplet with large deformation and high mass transfer rate, II: variable-density, variable-property case, J. Comput. Phys. 394 (2019) 1–17.
[18] J. Palmore, O. Desjardins, A volume of fluid framework for interface-resolved simulations of vaporizing liquid-gas flows, J. Comput. Phys. 399 (2019) 108954.
[19] J. Reutzsch, C. Kieffer-Roth, B. Weigand, A consistent method for direct numerical simulation of droplet evaporation, J. Comput. Phys. 413 (2020) 109455.
[20] N. Scapin, P. Costa, L. Brandt, A volume-of-fluid method for interface-resolved simulations of phase-changing two-fluid flows, J. Comput. Phys. 407 (2020) 109251.
[21] L. Germes Martinez, B. Duret, J. Reveillon, F.X. Demoulin, A new DNS formalism dedicated to turbulent two-phase flows with phase change, Int. J. Multiphase Flow 143 (2021) 103762.
[22] L. Bureš, Y. Sato, Direct numerical simulation of evaporation and condensation with the geometric VOF method and a sharp-interface phase-change model, Int. J. Heat and Mass Transfer 173 (2021) 121233.
[23] L.C. Malan, A.G. Malan, S. Zaleski, P.G. Rousseau, A geometric VOF method for interface resolved phase change and conservative thermal energy advection, J. Comput. Phys. 426 (2021) 109920.
[24] S. Zamani Salimi, N. Scapin, E. Popescu, P. Costa, L. Brandt, A Volume-of-fluid method for multicomponent droplet evaporation with robin boundary conditions, J. Comput. Phys. 514 (2024) 113211.
[25] E. Cipriano, A. Frassoldati, T. Faravelli, S. Popinet, A. Cuoci, et al., Multicomponent droplet evaporation in a geometric volume-of-fluid framework, J. Comput. Phys. 507 (2024) 112955.
[26] M.S. Dodd, A. Ferrante, A fast pressure-correction method for incompressible two-fluid flows, J. Comput. Phys. 273 (2014) 416–434.
[27] A. Baraldi, M.S. Dodd, A. Ferrante, A mass-conserving volume-of-fluid method: Volume tracking and droplet surface-tension in incompressible isotropic turbulence, Comput. & Fluids 96 (2014) 322–337.
[28] F. Gibou, R.P. Fedkiw, L.-T. Cheng, M. Kang, A second-order-accurate symmetric discretization of the Poisson equation on irregular domains, J. Comput. Phys. 176 (1) (2002) 205–227.
[29] G. Tryggvason, R. Scardovelli, S. Zaleski, Direct Numerical Simulations of Gas-Liquid Multiphase Flows, Cambridge University Press, 2011.
[30] M.S. Dodd, Direct Numerical Simulation of Droplet-Laden Isotropic Turbulence, Ph.D. thesis, 2017.
[31] T. Arrufat, M. Crialesi-Esposito, D. Fuster, Y. Ling, L. Malan, S. Pal, R. Scardovelli, G. Tryggvason, S. Zaleski, A mass-momentum consistent, Volume-of-Fluid method for incompressible flow on staggered grids, Combust. and Flame 215 (2021) 104785.
[32] J. López, J. Hernández, Analytical and geometrical tools for 3D volume of fluid methods in general grids, J. Comput. Phys. 227 (12) (2008) 5939–5948.
[33] S. Dong, J. Shen, A time-stepping scheme involving constant coefficient matrices for phase-field simulations of two-phase incompressible flows with large density ratios, J. Comput. Phys. 231 (17) (2012) 5788–5804.
[34] J.U. Brackbill, D.B. Kothe, C. Zemach, A continuum method for modeling surface tension, J. Comput. Phys. 100 (2) (1992) 335–354.
[35] S. Chen, D.B. Johnson, P.E. Raad, Velocity boundary conditions for the simulation of free surface fluid flow, J. Comput. Phys. 116 (2) (1995) 262–276.
[36] G. Valori, B. Kliem, R. Keppens, Extrapolation of a nonlinear force-free field containing a highly twisted magnetic loop, Astron. & Astrophys. 433 (1) (2005) 335–347.
[37] M.S. Dodd, A. Ferrante, On the interaction of Taylor lengthscale size droplets and isotropic turbulence, J. Fluid Mech. 806 (2016) 356–412.
[38] H.S. Udaykumar, R. Mittal, W. Shyy, Computation of solid–liquid phase fronts in the sharp interface limit on fixed grids, J. Comput. Phys. 153 (2) (1999) 535–574.
[39] B. Fornberg, Generation of finite difference formulas on arbitrarily spaced grids, Math. Comput. 51 (184) (1988) 699–706.
[40] M. Sussman, A second order coupled level set and volume-of-fluid method for computing growth and collapse of vapor bubbles, J. Comput. Phys. 187 (1) (2003) 110–136.
[41] A. Prosperetti, Motion of two superposed viscous fluids, Phys. Fluids 24 (1981) 1217.
[42] D.B. Spalding, The combustion of liquid fuels, In Proc. Fourth Symp. (Intl) on Combustion (1953) 847–864.
[43] N. Wilkins-Diehr, S. Sanielevici, J. Alameda, J. Cazes, L. Crosby, M. Pierce, R. Roskies, An Overview of the XSEDE Extended Collaborative Support Program, Springer International Publishing, Cham, 2016, pp. 3–13.